

Reionization in Technicolor

Kristian Finlator^{1,8,11}, Laura Keating², Benjamin D. Oppenheimer⁴, Romeel Davé^{5,6,7,9,10}, Erik Zackrisson³

¹ *New Mexico State University, Las Cruces, NM, USA*

² *Canadian Institute for Theoretical Astrophysics, 60 St. George Street, University of Toronto, ON M5S 3H8, Canada*

³ *Department of Physics and Astronomy, Uppsala University, 751 20 Uppsala, Sweden*

⁴ *CASA, Department of Astrophysical and Planetary Sciences, University of Colorado, 389-UCB, Boulder, CO 80309, USA*

⁵ *University of the Western Cape, Bellville, Cape Town 7535, South Africa*

⁶ *South African Astronomical Observatory, Observatory, Cape Town 7925, South Africa*

⁷ *African Institute for Mathematical Sciences, Muizenberg, Cape Town 7945, South Africa*

⁸ *Cosmic Dawn Center (DAWN), Niels Bohr Institute, University of Copenhagen / DTU-Space, Technical University of Denmark*

⁹ *Center for Computational Astrophysics, Simons Foundation, New York, NY 10010, USA*

¹⁰ *Institute for Astronomy, Royal Observatory, Edinburgh EH9 3HJ, UK*

¹¹ *finlator@nmsu.edu*

Accepted XXX. Received YYY; in original form ZZZ

ABSTRACT

We present the *Technicolor Dawn* simulations, a suite of cosmological radiation-hydrodynamic simulations of the first 1.2 billion years. By modeling a spatially-inhomogeneous UVB on-the-fly with 24 frequencies and resolving dark matter halos down to $10^8 M_\odot$ within $12h^{-1}\text{Mpc}$ volumes, our simulations unify observations of the intergalactic and circumgalactic media, galaxies, and reionization into a common framework. The only empirically-tuned parameter, the fraction $f_{\text{esc,gal}}(z)$ of ionizing photons that escape the interstellar medium, is adjusted to match observations of the Lyman- α forest and the cosmic microwave background. With this single calibration, our simulations reproduce the history of reionization; the stellar mass-star formation rate relation of galaxies; the number density and metallicity of damped Lyman- α absorbers (DLAs) at $z \sim 5$; the abundance of weak metal absorbers; the ultraviolet background (UVB) amplitude; and the Lyman- α flux power spectrum at $z = 5.4$. The galaxy stellar mass and UV luminosity functions are underproduced by $\leq 2\times$, suggesting an overly vigorous feedback model. The mean transmission in the Lyman- α forest is underproduced at $z < 6$, indicating tension between measurements of the UVB amplitude and Lyman- α transmission. The observed Si IV column density distribution is reasonably well-reproduced ($\sim 1\sigma$ low). By contrast, C IV remains significantly underproduced despite being boosted by an intense > 4 Ryd UVB. Solving this problem by increasing metal yields would overproduce both weak absorbers and DLA metallicities. Instead, the observed strength of high-ionization emission from high-redshift galaxies and absorption from their environments suggest that the ionizing flux from conventional stellar population models is too soft.

Key words: reionization — galaxies: formation — galaxies: evolution — galaxies: high-redshift — intergalactic medium — quasars: absorption lines

1 INTRODUCTION

The first billion years of cosmological time witnessed a number of physical transformations that will constitute the subject of detailed scrutiny over the next decade: The formation of the first stars, galaxies, and quasars; the enrichment and heating of the circumgalactic medium (CGM) owing to feedback processes occurring deep within galaxies; and the transformation of the intergalactic medium (IGM) from a cold, neutral medium

into a hot, ionized one. Dedicated observational campaigns are now probing separately the CGM around early galaxies (D’Odorico et al. 2013; Bosman et al. 2017; Chen et al. 2017b); the nature of their stellar populations (Steidel et al. 2016; Smit et al. 2017; Berg et al. 2018); and the IGM’s temperature (Viel et al. 2013a; Garzilli et al. 2017) and ionization state (Calverley et al. 2011; Wyithe & Bolton 2011; Davies et al. 2018b; D’Aloisio et al. 2018).

Physical insight into what these observations imply is being pursued through a variety of theoretical approaches,

2 The Technicolor Dawn Simulations

which are usually optimized separately to address a small subset of available observations (Trac & Gnedin 2011). These dedicated efforts have unearthed several problems that seem resistant to solution. For example, models that match the reported amplitude of the extragalactic ultraviolet background (UVB) at $z = 5.4$, often quantified by the hydrogen photoionization rate Γ_{HI} , underproduce the mean transmission in the Lyman- α forest (Bosman et al. 2018). Moreover, assuming a model for the UVB that matches the observed Γ_{HI} nearly invariably leads to underproducing the CGM's CIV abundance at $z > 3$ (Rahmati et al. 2016; Keating et al. 2016; Turner et al. 2016). Both of these observations hint at the need for a more intense UVB or a hotter IGM, perhaps the result of a harder ionizing continuum (D'Aloisio et al. 2015; Keating et al. 2018). Such a revision would also modulate the predicted abundance of low-ionization metal absorbers and damped Lyman- α absorbers (DLAs; Rafelski et al. 2014; Bird et al. 2017). Can a single model satisfy all of these constraints, or are the observations fundamentally in tension with one another? If indeed it turns out that a more intense UVB yields generally improved agreement with observations, can it be attributed to the observed level of early star formation given standard stellar population synthesis models, or are updates required for the physics of young, low-metallicity stars (Stanway et al. 2016; Rosdahl et al. 2018)?

In the current, data-rich era, it is worth considering whether combining observations that are traditionally considered separately can yield new insights when subsumed within a single theoretical framework. This work takes the view that the critical link is the UVB, which couples stars, the CGM, and the IGM. A generation of theoretical studies has modeled the IGM and CGM during the hydrogen reionization epoch under the assumption of a spatially-homogeneous, externally-imposed UVB, usually coupled with the assumption that gas is in ionization equilibrium (Oppenheimer et al. 2009; Lukić et al. 2015; Keating et al. 2016). Both assumptions are inaccurate: reionization is directly observed to be a spatially-inhomogeneous process (Becker et al. 2015b; Bosman et al. 2018) that is generally believed to have been driven by ionizing flux from small galaxies (Finlator et al. 2016; D'Aloisio et al. 2017; Parsa et al. 2018; Qin et al. 2017; McGreer et al. 2018; Hassan et al. 2018), although a significant contribution from rare, bright sources remains possible (Chardin et al. 2015; Madau & Haardt 2015). Treating reionization as a spatially-homogeneous process severs its links to the sources that drove it. Moreover, it limits the ability of models to address small-scale tracers of reionization such as metal absorbers or small-scale fluctuations in the Lyman- α flux power spectrum. This is even more true when high-ionization absorbers such as CIV are considered because they are sensitive to He II-ionizing photons, which were not homogeneously distributed until the close of He II reionization around $z = 2.7$ (Worseck et al. 2016). Meanwhile, forcing the diffuse IGM into ionization equilibrium boosts the HI fraction and the collisional excitation cooling rate, leading to an artificially-cold IGM (Puchwein et al. 2015).

Reionization affects overdense and underdense regions in different ways and at different times (Finlator et al. 2009), hence it is important to consider how measurements that

probe the diffuse and condensed gas phases complement one another. The physical state of the IGM is most readily probed through observations of the Lyman- α forest (LAF) while material that is associated with galaxy formation (that is, the CGM) is probed through observations of metal absorbers and DLAs. Modeling these media simultaneously is useful for two reasons. First, at $z > 5$, the LAF probes primarily underdense IGM gas while the CGM probes overdense gas; the two phases therefore provide complementary probes that can be combined to gain insight into the topology of reionization. Second, whereas the LAF is an exquisite probe of the post-reionization IGM (Becker et al. 2015a; McQuinn 2016), it saturates at $z > 6$, leaving metal absorbers as the only viable probe of the UVB's growth at earlier times (Oh 2002; Keating et al. 2014, 2016). This indicates the need for theoretical models that can make the connection between observables that track the progress of reionization before and after $z = 6$.

Metal absorbers are more than just a complicated substitute for the LAF, however: given their proximity to galaxies, they are the *most direct* observational probe of the galaxy-driven reionization hypothesis: they probably trace activity in the faint—currently unobservably so—systems that dominated reionization (Díaz et al. 2014; Cai et al. 2017), and their physical state bears the chemical and radiative signatures of outflows and ionizing flux from the young stars in those galaxies.

Combining these arguments leads to the need for radiation-hydrodynamic simulations of the reionization epoch with realistic star formation histories and metal yields as well as a spatially-inhomogeneous, multifrequency UVB. In this way, observations of all baryon phases can be treated as complementary tracers of the progress of reionization. As a step in this direction, we present the *Technicolor Dawn* simulations. At small scales, these simulations adopt subgrid prescriptions for star formation and feedback that, while heavily updated to incorporate insight from observations and complementary modeling efforts, are directly descended from the pathbreaking framework presented in Springel & Hernquist (2003). This means that gas inflows into galaxies, star formation, enrichment, and feedback are modeled in a way that allows predictions of bulk galaxy properties such as stellar mass, star formation rate, color, metallicity, and environment. The UVB, however, is modeled using an on-the-fly radiation transport solver using 24 independent frequency bins. The physical conditions of the CGM and—crucially for reionization—the IGM are treated self-consistently, with the result that the detailed way in which the IGM is heated, pressurized, and enriched connects directly to the underlying model for galaxy growth. In the process, it allows us to address simultaneously observations of galaxies, the CGM, and the IGM and evaluate whether their implications are mutually consistent.

In Section 2, we present an overview of the *Technicolor Dawn* simulations. In Section 3, we present initial results. In Section 4, we summarize and discuss our results.

2 SIMULATION

Our simulations assume a *Planck* cosmology (Planck Collaboration et al. 2016a) in which

$(\Omega_M, \Omega_\Lambda, \Omega_b, H_0, X_H) = (0.3089, 0.6911, 0.0486, 67.74, 0.751)$. Initial conditions are generated at $z = 199$ using MUSIC (Hahn & Abel 2011). They incorporate an extensive suite of updates with respect our previous work, hence we review our physical model in detail.

2.1 Hydrodynamics and Star Formation

We run our simulations using a custom version of GADGET-3 (last described in Springel 2005). Hydrodynamics are modelled using a density-independent formulation of smoothed particle hydrodynamics (SPH) that treats fluid instabilities accurately (Hopkins 2013). We compute the physical properties of each gas particle using a 5th-order B-spline kernel that incorporates information from up to 32 neighbours. Increasing the minimum number of neighboring particles leads to a more accurate hydrodynamic calculation, but it also suppresses star formation in low-mass systems at early times, hence we retain the coarser kernel for the present.

Gas particles cool radiatively owing to collisional excitation of hydrogen and helium using the processes and rates in Table 1 of Katz et al. (1996). In the case of our radiation transfer simulations, however, we relax the assumption that hydrogen and helium are in ionization equilibrium. Gas particles that have nonzero metal mass fraction are further allowed to cool via collisional excitation of metals cooling using the collisional ionization equilibrium tables of Sutherland & Dopita (1993).

Gas whose proper hydrogen number density exceeds 0.13 cm^{-3} acquires a subgrid multiphase structure (Springel & Hernquist 2003) and forms stars at a rate that is calibrated to match the observed Kennicutt-Schmidt law. We assume that stars form with a universal Kroupa (2001) initial mass function (IMF) from $0.1\text{--}100M_\odot$ (although this may underpredict the mass fraction in even more massive stars; Crowther et al. 2016; Schneider et al. 2018). We assume that all stars more massive than $10M_\odot$ end their lives instantaneously as supernovae (SNe), implying a SN mass fraction of 0.187 ($= \beta$ in Springel & Hernquist 2003). Following Nomoto et al. (2006), we further assume that half of SNe are hypernovae and that SNe from stars more massive than $50M_\odot$ do not release metals into the ISM. With these assumptions, we find that SNe release 3.75×10^{49} ergs of energy per M_\odot of new stars. This is an order of magnitude more feedback energy than is assumed in Springel & Hernquist (2003), but we leave the local heating parameter u_{SN} unchanged. This corresponds to the assumption that most of the feedback energy is radiated away or converted efficiently to kinetic energy associated with galactic outflows.

2.2 Metal Enrichment

Our simulations independently model metal enrichment of C, O, Si, Fe, N, Ne, Mg, S, Ca, and Ti. We compute the Type II SNe metal yields by weighting the supernovae yields of Nomoto et al. (2006) by our assumed IMF and assuming a 50% hypernovae (HNe) fraction. Each star-forming particle’s Type II self-enrichment rate is then obtained by interpolating to its metallicity. The resulting assumed metal yields are in Table 2.

As is well-known, the metal yields are a source

of uncertainty in cosmological simulations, with \sim factor of two variations among yields that are commonly assumed (Wiersma et al. 2009). In order to estimate how the unknown HNe fraction contributes to our metal production, we recompute our metal yields for a $Z = 0.001$ stellar population with assumed HNe fractions of 0, 0.5, and 1.0 in Table 3 (note that typical star-forming gas at $z = 6$ has a metallicity of $Z \sim 0.1Z_\odot$). Broadly, HNe in low-metallicity stars boost the yields of C, O, Si, Fe, N, Ne, Mg, and Ti by factors of up to 65% (in the case of Ti). By contrast, they suppress the yields of S and Ca by up to 10–15%. Evidence that the boosted yields may be realistic comes from the fact that simulations without HNe often underproduce the normalization of the mass-metallicity relation, which is generally calibrated to the oxygen mass fraction (Somerville & Davé 2015; Davé et al. 2016). Hence while the unknown HNe fraction contributes an overall uncertainty of 2–50% to our enrichment model (depending on the species), the addition of HNe may alleviate some tension between simulations and observations.

We model enrichment from Type Ia SNe assuming a continuous Heringer et al. (2017) delay time distribution: A stellar population of age t has a Type Ia rate \dot{N}_{Ia} of

$$\dot{N}_{\text{Ia}} = 3.2 \times 10^{-13} \left(\frac{t}{\tau}\right)^{-1.5} M_\odot^{-1} \text{yr}^{-1}. \quad (1)$$

Metal yields from Type Ia SNe are adopted from the W7 model in Table 2 of Maeda et al. (2010).

Star particles that are old enough to form asymptotic giant branch (AGB) stars lose mass and metals to the nearest gas particle. The metal content in C, O, and N is enhanced with respect to the star particle’s original metallicity whereas the metal mass fraction in all other species is unchanged; see Oppenheimer & Davé (2008) for details.

2.3 Feedback

Galactic outflows form via a Monte Carlo model in which star-forming gas particles receive “kicks” in momentum space and are thereafter temporarily decoupled hydrodynamically. The probability that a star-forming gas particle is ejected at any timestep depends on its star formation rate and its host galaxy’s stellar mass in a way that is tuned to match the ratio η_{W} of the mass outflow rate to the star formation rate predicted from high-resolution simulations (Muratov et al. 2015, their Equation 8)¹:

$$\eta_{\text{W}}(M_*) = 3.6(M_*/10^{10}M_\odot)^{-0.35}. \quad (2)$$

While the Muratov et al. (2015) mass-loading factor seems to have substantial predictive power (Davé et al. 2016; Fontanot et al. 2017), we have found that directly adopting their outflow velocities (their Equation 9) leads to very little gas escaping the host galaxy. Accordingly, we follow Davé et al. (2016) and add two boost factors. The first accounts for the fact that stars characteristically form at a halocentric radius of 0.034 times the virial radius

¹ We have also experimented with the dependence on halo mass and redshift that they give in their Equations 4 and 5 but found that this drastically over-suppresses star formation at high redshift.

4 The Technicolor Dawn Simulations

R_{vir} (Huang et al. 2017) whereas the reported outflow scalings correspond to $0.25R_{\text{vir}}$. We account for this energy loss ΔE by assuming the host halo, whose mass is computed by an on-the-fly group finder, has a Navarro et al. (1996) density profile with a concentration given by the concentration-mass relation of Angel et al. (2016). The second is a multiplicative factor that insures that some of the gas is boosted up to velocities approaching 3 times the circular velocity, as observed (Chisholm et al. 2015). The final adopted velocity scaling is

$$v = 2.3485v_c^{1.12} + \Delta E \quad (3)$$

where v_c is the circular velocity in km s^{-1} . We multiply each outflowing particle's velocity by a random number drawn uniformly from the range [0.75, 1.25].

Equation 3 yields a median velocity that exceeds predictions from high-resolution simulations (Equation 10 of Muratov et al. 2015). However, the energy requirements for powering these outflows do not greatly exceed the energy available from Type II SNe. For a constant stellar baryon fraction $M_*/M_b = 0.1$, the ratio of the wind kinetic energy to the Type II SNe energy scales with the halo mass as $M_h^{0.4}$ and exceeds unity for halos more massive than $\log(M_h/M_\odot) = (11.4, 10.9)$ at $z = (6, 10)$. It does not exceed 3 for any halo less massive than $10^{12}M_\odot$ during the same epoch. Given the order-of-magnitude uncertainty in the available energy from SNe, the fact that halos more massive than $10^{11}M_\odot$ do not form by $z = 6$ in our modest simulation volumes, and the possible contribution of other processes such as stellar winds, we do not believe that this energy requirement is excessive. Nonetheless, we will show in Figures 16–17 that the abundance of weak low-ionization absorbers may be overproduced in our model, which may indicate that more moderate outflow velocities are indeed preferred (see also Keating et al. 2016).

As our simulations do not resolve the ISM with sufficient detail to treat the emergence of outflows self-consistently, we retain the convention of hydrodynamically decoupling gas that is kicked into outflows (Springel & Hernquist 2003). Gas recouples once its density falls to 10% of the minimum density for star formation, or after a time delay equal to the host halo's virial radius divided by the gas particle's initial kick velocity. The virial radius is derived from the halo mass combined with the Bryan & Norman (1998) fitting-formula for virial overdensity as a function of redshift.

2.4 Radiation Transport

A key ingredient in our effort to model realistically the photoionization feedback that occurs at $z > 5$ is the inclusion of a self-consistent, inhomogeneous, multifrequency UVB. We model the evolving UVB on-the-fly by solving the moments of the radiation transport (RT) equation on a uniform Cartesian grid that is superposed on our simulation volume (Finlator et al. 2009). We discretize the radiation field owing to galaxies spatially on a regular grid and spectrally into 24 frequency groups spaced evenly between 1–10 Ryd. The quasar field is spatially uniform except for the subgrid self-shielding prescription (see below) but evolved in the same frequency bins using the volume-averaged opacity field.

2.4.1 Limiting Cosmological Redshifting

A multifrequency radiation transport solver allows us to account for cosmological redshifting, but our numerical implementation requires us to limit this effect in order to avoid introducing numerical noise when computing the derivative of the intensity. To see this, we integrate over the cosmological radiation transport equation (for example, Gnedin & Ostriker 1997; Finlator et al. 2009) in frequency to yield a multigroup method:

$$\frac{\partial I}{\partial t} = \frac{-cn^i}{a} \frac{\partial I}{\partial x^i} + c\eta_i - c \left[\chi + \frac{H}{c} \left(2 - \frac{1}{I} \int v \frac{\partial I_v}{\partial v} dv \right) \right] I \quad (4)$$

Here, I_v is the proper photon number density per unit frequency; $I = \int I_v dv$ is the density in a particular frequency bin; n^i is the i th component of a unit vector; a is the cosmological expansion factor; c is the speed of light; η_i is the ionizing emissivity; $H = \dot{a}/a$ is the cosmological expansion rate; and χ is the photoelectric opacity. The term with the prefactor (H/c) is the cosmological term. This functions as an opacity χ_H that accounts for both dilution and redshifting. Carrying out the integral over a frequency bin from ν_1 to ν_2 yields

$$\chi_H \equiv \frac{H}{c} \left[3 - \frac{1}{I} (\nu_2 I_\nu(\nu_2) - \nu_1 I_\nu(\nu_1)) \right]. \quad (5)$$

If the photon number density can be approximated as a power-law $I_\nu \propto \nu^{-\alpha}$, then this reduces to

$$\chi_H \equiv \frac{H}{c} [3 - (1 - \alpha)] \quad (6)$$

To understand Equation 6, consider the case of a uniform, flat-spectrum field with no sources and sinks; that is, $\alpha = \eta_i = \chi = 0$. In this case, the number density I of photons in a fixed energy bin evolves at a rate $\partial I/\partial t = -2H$. I evolves more slowly than the proper hydrogen number density ($\partial n_H/\partial t = -3H$) because photons gradually accumulate into bins of fixed width in energy. If we allow $\alpha > 0$, then there are fewer high-energy than low-energy photons and cosmological redshifting moves more energy out of the bin than into it, leading to more rapid dimming than in the flat-spectrum case. By contrast, if $\alpha < 0$, then the UVB's spectral slope is locally-hard and redshifting moves more energy into the bin than in the flat-spectrum case.

Trouble arises because we compute α numerically using the difference between the photon densities in successive frequency bins. When I_ν is small enough, numerical noise can lead to spuriously large values of $|\alpha|$. We find that enforcing $\alpha \geq -10$ suppresses the problem adequately.²

2.4.2 The Galaxy UVB

The galaxy emissivity field is computed from the star formation rate of star-forming gas particles, which improves spatial resolution with respect to models that derive the emissivity directly from star particles (Rahmati et al. 2013).

² In principle, this approximation smooths over sharp spectral features such as the sawtooth absorption spectrum from the He II Lyman series. However, this does not affect our current work because our model for the photoelectric opacity does not yet account for bound-bound transitions.

Each gas particle’s emissivity is proportional to its instantaneous star formation rate, which is assumed to have been constant for the past 100 Myr. The emissivity’s metallicity dependence is computed from a modified version of YGDRASIL (Zackrisson et al. 2011). The emissivity is tabulated at 7 distinct metallicities between $Z = 0$ –0.04, and each gas particle’s actual emissivity is computed by interpolating to its Z . The $Z = 0$ emissivity comes from Schaerer (2002); the $Z = 10^{-5}$ and $Z = 10^{-7}$ emissivities come from Raiter et al. (2010); and the $Z = 0.001$ –0.040 emissivities come from Starburst 99 (Leitherer et al. 1999), running with the Geneva tracks (high mass-loss version, without rotation) and Pauldrach/Hillier atmospheres. Each model is adjusted to a Kroupa (2001) IMF from 0.1– $100M_{\odot}$, consistent with our simulation’s star formation model.

In order to close the moment hierarchy, we use a time-independent ray-casting calculation to compute the Eddington tensor field separately for each frequency bin. After each timestep, any “target” cell in which the radiation field in at least one frequency bin changes by a factor greater than 100% is flagged for update. A ray-tracing code then computes the total optical depth from the target cell to each source cell. Periodic boundary conditions are accounted for by replicating the simulated emissivity and opacity fields in 26 replicas that surround the actual computation volume. In other words, each source gives rise to 27 ray-casting calculations per target cell. To save computation time, we halt ray-casting calculations whenever the optical depth from the target cell to the source cell exceeds 6 in all frequency bins. The local Eddington tensor field is then computed based on the contribution from those sources that were unobscured. Note that this calculation is not used to compute the actual radiation field, which results from solving the moments of the RT equation.

Even with these optimizations, the computation time for Eddington tensor updates scales too severely with the problem’s dynamic range. To tame this problem, we compute Eddington tensor updates on a coarse grid. For example, for simulations that include 64^3 RT voxels, we smooth the simulated opacity and emissivity fields onto an 8^3 grid (where each coarse grid cell contains 512 RT voxels), compute the updated Eddington tensors on the coarse grid, and then assume that the Eddington tensor field is uniform throughout each coarse grid cell. The price for such approximations is the introduction of small errors in the shapes of HII regions at early times (Gnedin & Abel 2001), but the impact on the overall history of reionization is expected to be weak.

At each timestep, the UVB is used to evolve each particle’s H and He ionization states forward, and the resulting opacity field is used to evolve the UVB. The opacity field accounts only for bound-free transitions in HI, He I, and He II. An iterative solver repeats the ionization and moment updates throughout the simulation volume if the UVB changes over the course of a timestep in at least one voxel and frequency by more than 1%. If the iteration does not yield a converged UVB within 1% at all frequencies and locations within 10 iterations, then a substepper collapses the timestep and evolves the UVB and ionization fields forwards at the reduced timestep, iterating to 1% convergence at each substep as before.

A chemical courant condition attempts to capture the

progress of ionization fronts by limiting a particle’s timestep to $\tau_e = 0.5n_e/\dot{n}_e$ (where n_e is the local electron density and its derivative includes all contributions from ionizations and recombinations of H and He). Unfortunately, n_e/\dot{n}_e drops to extremely short values at ionization fronts, which can grind the simulation to a halt. We therefore impose a lower limit $\tau_e \geq 100,000$ years; in other words, an individual particle’s timestep may not be cut shorter than this owing to the chemical courant condition. This smooths ionization fronts over a spatial scale of order $c\tau_e \sim 30\text{kpc}$, which is comparable to the spatial resolution of our radiation transport solver. The fully-implicit ionization solver can treat evolution on timesteps larger than n_e/\dot{n}_e robustly.

For our highest-resolution simulation ($12h^{-1}\text{Mpc}$ volume with 64^3 RT voxels), each voxel has a side length equal to 1/64th of the total simulation volume, or $187.5\text{ comoving }h^{-1}\text{kpc}$. This means that, throughout the reionization epoch ($z > 6$), the radiation field is directly resolved down to scales of < 50 physical kpc. This remains too coarse to resolve the escape of ionizing radiation from galaxies’ interstellar media and somewhat too large to resolve self-shielding within Lyman-limit systems, hence we employ two further prescriptions to account for subgrid effects: one accounts for UVB attenuation as it penetrates into dense regions from the outside, and one accounts for absorption of locally-produced light as it exits dense star-forming regions.

The first, a self-shielding prescription that generalizes ideas originally presented in Schaye (2001) and Haehnelt et al. (1998), attenuates the UVB in dense regions based on the assumption that dense gas is in hydrostatic and photoionization equilibrium (see section 2.2 of Finlator et al. 2015 for details). The assumption of photoionization equilibrium is invoked only to compute the self-shielding. Once the locally-attenuated UVB is computed, it is used to evolve the gas’ ionization state via a nonequilibrium solver. The contribution of self-shielded gas particles to the local opacity is reduced by the same factor as the local UVB; that is, if the UVB in a particular frequency is suppressed by 90% owing to self-shielding, then that particle’s contribution to the local opacity in that frequency is likewise reduced by 90% with respect to the optically-thin case. This treatment has no free physical parameters and yields excellent agreement with high-resolution calculations that resolve ionization fronts at IGM filaments (Finlator et al. 2015).

Our second treatment for subgrid radiation transport effects involves the fraction $f_{\text{esc,gal}}$ of ionizing photons that escape from galaxies, which is much more difficult to model. Good agreement with observations of the Thomson scattering optical depth and the observed ionizing emissivity at $z \leq 6$ are generally obtained by arguing that $f_{\text{esc,gal}}$ could increase either to low masses (Alvarez et al. 2012; Wise et al. 2014) or luminosities (Paardekooper et al. 2015; Sharma et al. 2016), or—perhaps equivalently—to high redshift (Haardt & Madau 2012; Kuhlen & Faucher-Giguère 2012; Khaire et al. 2016; Doussot et al. 2017). The most general model for $f_{\text{esc,gal}}$ would permit dependence on the galaxy’s mass and luminosity as well as its recent star formation history and ISM structure (Ma et al. 2015; Paardekooper et al. 2015; Katz et al. 2018). Unfortunately, despite over a decade of effort, the way in which $f_{\text{esc,gal}}$ varies with these factors is not yet robustly constrained. Moreover, our simulations do not resolve the ISM-scale processes

6 The Technicolor Dawn Simulations

that determine $f_{\text{esc,gal}}$ (Ma et al. 2015). Consequently, in this work we follow Haardt & Madau (2012) and consider a pure redshift dependence $f_{\text{esc,gal}}(z)$:

$$f_{\text{esc,gal}}(z) = 0.176 \left(\frac{1+z}{6} \right)^A \quad (7)$$

We also cap $f_{\text{esc,gal}}$ at a value $f_{\text{esc,max}}$, leading to a constant $f_{\text{esc,gal}}$ at sufficiently high redshifts.

This model for $f_{\text{esc,gal}}$ contains three parameters: a normalization, a slope, and a maximum. These parameters are adjusted in three steps. First, the normalization is fixed to a constant value in order to match roughly the observationally-inferred ionizing emissivity at $z = 5$ (for example, Table 2 of Kuhlen & Faucher-Giguère 2012). Next, we run a simulation with a trial model for $f_{\text{esc,gal}}$ in order to establish how many photons per hydrogen atom are required to bring the volume-averaged neutral fraction $X_{\text{H I,V}}$ below 1%. This number depends mostly on the simulation’s resolution rather than on the model for $f_{\text{esc,gal}}(z)$. Finally, we evaluate a broad range of combinations of A and $f_{\text{esc,max}}$ in post-processing to determine which ones emit enough ionizing photons to complete reionization by $z = 6$. This calibration step involves integrating the product of the comoving star formation rate density $\dot{\rho}_*$ from the trial simulation with a representative ionizing efficiency and each combination of A and $f_{\text{esc,max}}$, and then integrating in time:

$$n_\gamma(t) = \int_0^t \dot{\rho}_*(t') Q f_{\text{esc,gal}}(z(t')) dt' \quad (8)$$

Here, $n_\gamma(t)$ is the cumulative number of ionizing photons emitted into the IGM per unit volume by time t , and Q is the ionizing efficiency in photons $\text{sec}^{-1} M_\odot^{-1} \text{yr}$. While Q varies self-consistently with the local metallicity in “live” simulations, we have found that $\log(Q) = 53.51$ approximates the predicted volume-averaged emissivity reasonably well.

The final choice of A and $f_{\text{esc,max}}$ involves fitting two parameters to one measurement and thus introduces a measure of freedom. Without further observational guidance, we favor combinations that do not involve either large $f_{\text{esc,max}}$ or the rapid evolution in $f_{\text{esc,gal}}$ that occurs when $A > 3.5$. In principle, measurements of the duration of hydrogen reionization can reduce this freedom (Doussot et al. 2017); however, we have not considered this.

The number of ionizing photons per hydrogen atom that must be emitted in order for reionization to complete depends on the resolution of our radiation transport solver: For a $12h^{-1}\text{Mpc}$ box with 2×256^3 particles, simulations in which the RT voxels have a comoving side length of (375, 187.5) $h^{-1}\text{kpc}$ emit (2.44, 3.02) ionizing photons per hydrogen atom before $X_{\text{H I,V}}$ drops below 1%. The slight lack of convergence is expected: If the resolution is higher, then fewer absorptions occur at subgrid scales, and $f_{\text{esc,gal}}$ must be higher. Likewise, the total number of photons per baryon that are absorbed at scales larger than the grid scale increases. In order for our simulations to yield consistent reionization histories, we therefore allow $f_{\text{esc,gal}}(z)$ to vary with resolution so that $A = (1.95, 3.4)$ and $f_{\text{esc,max}} = (0.36, 0.5)$ for the same resolutions (see Table 1). We expect that the preferred redshift dependence will weaken as we scale up to larger volumes. This is because because periodic cosmological volumes that are smaller than $\sim 100h^{-1}\text{Mpc}$ experience artificially sudden reionization histories owing to their lack of large-scale

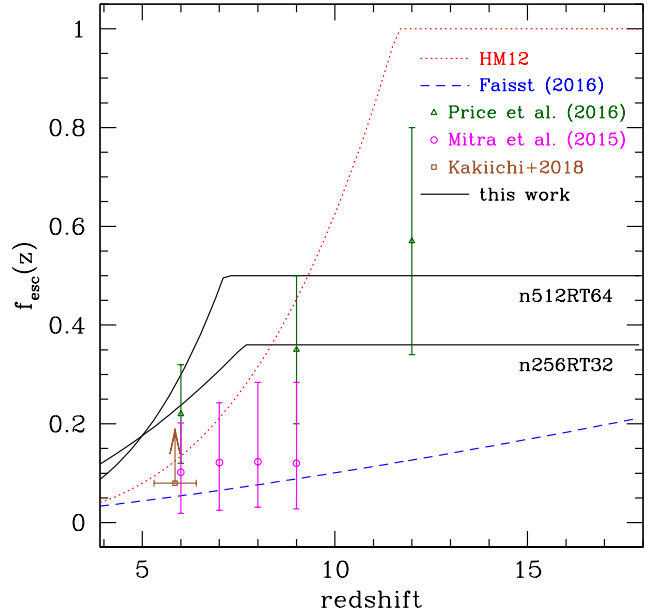


Figure 1. Our adopted models for $f_{\text{esc,gal}}(z)$ versus several other models from the literature. Our simulations adopt values of $f_{\text{esc,gal}}$ that are consistent with inferences from semi-analytical models but slightly higher than more direct observational inferences. They also require higher $f_{\text{esc,gal}}$ if the resolution of the radiation transport solver is higher, as indicated by the numbers beneath the solid curves.

density fluctuations (Barkana & Loeb 2004; Iliev et al. 2014; Doussot et al. 2017), which we effectively compensate for via a large $f_{\text{esc,gal}}$ at earlier times.

In Figure 1, we compare our model for $f_{\text{esc,gal}}(z)$ versus other recent determinations. Our simulations assume a volume-averaged $f_{\text{esc,gal}}$ that exceeds what is assumed by the Haardt & Madau (2012) model for $5 < z < 9$, but is lower at earlier times. At all redshifts, the adopted dependence is consistent with what Price et al. (2016) infer when using a non-parametric analysis to match the *Planck* 2015 TT,TE,EE+lowP measurements using the Bouwens et al. (2015) UV luminosity function. The disagreement with respect to the complementary semi-analytical modeling by Mitra et al. (2015) is more pronounced, likely reflecting an overall lower $\dot{\rho}_*$ in our model (see Figure 3). Perhaps more troublingly, the purely-observational inference on the mean escape fraction of galaxies with stellar mass $M_* = 10^9 M_\odot$ based on H α observations by Faisst (2016) is lower than any of the models that are tuned to reproduce reionization. This includes inferences from updated analytical models, which tend to require $f_{\text{esc}} > 0.1$ (Madau 2017). While galaxies with $f_{\text{esc}} \geq 0.4$ have been reported (Izotov et al. 2018; Vanzella et al. 2018), they do not seem to be the norm. On the other hand, they are consistent with the lower limit of 0.08 recently inferred from observations of transmissive regions along a sightline to a $z = 6.42$ QSO (Kakiichi et al. 2018), which in turn is slightly inconsistent with Faisst (2016). Our work reinforces the already well-known tension between direct observations of ionizing photon escape and the requirements of reioniza-

tion (see also Rutkowski et al. 2017). We return to this point in Section 4.2.

2.4.3 The Quasar UVB

The space density of bright quasars (QSOs) is too low for a representative number of them to occur in our limited simulation volumes (see also Gnedin 2014). Nonetheless, their contribution must be included as they account for an increasing fraction of the total flux at lower redshifts ($z < 5$) and high energies ($h\nu > 4$ Ryd). We model the QSO UVB as a spatially-homogeneous field, appropriate for the case in which they are predominantly distant, using a volume-averaged radiation transport calculation.

We take the emissivity at 1 Ryd as a function of redshift from Equation 9 of Manti et al. (2017) and assume that quasars make no contribution above $z = 8$. We use the Lusso et al. (2015) continuum slope to obtain the emissivity at higher energies. This leaves only the question of what fraction $f_{\text{esc,QSO}}$ of ionizing photons escape into the IGM. While it is traditionally assumed that $f_{\text{esc,QSO}} = 1$ (for example, Haardt & Madau 2012), in principle it is possible that $f_{\text{esc,QSO}}$ varies with luminosity and redshift for QSOs just as in the case of galaxies. Indeed, recent observations indicate that $f_{\text{esc,QSO}} \approx 0.7$ in the case of bright QSOs at $z \sim 3$ (Cristiani et al. 2016). Furthermore, Micheva et al. (2017) report observations of 14 faint QSOs at $z \sim 3$ that are consistent with much lower values for $f_{\text{esc,QSO}}$ (including zero). At slightly higher redshift, Grazian et al. (2018) find $0.44 < f_{\text{esc,QSO}} < 1.0$ with a mean value of $\langle f_{\text{esc,QSO}} \rangle = 0.74$ for 16 faint AGN at $z > 4$. Hence while it is becoming clear that $f_{\text{esc,QSO}} < 1$, there is not yet observational guidance as to what one should adopt for $f_{\text{esc,QSO}}$ in the case of high-redshift QSOs. For the present, we key off of Cristiani et al. (2016) and assume that $f_{\text{esc,QSO}} = 70\%$ for QSOs as an ensemble. In the long term, it may be that joint observations of QSOs and the IGM are needed to infer $f_{\text{esc,QSO}}$, just as in the case of galaxies.

At each iteration of our radiation-ionization solver, we update the simulation's QSO UVB via Equation 1 of Haardt & Madau (2012). We adopt for the QSO opacity the volume-averaged opacity as a function of frequency over our entire simulation volume. The QSO UVB's ability to ionize and heat dense gas is suppressed via our subgrid self-shielding prescription in the same way as the galaxy UVB.

2.5 Assumptions versus Predictions

While the goal of cosmological simulations is to compute as much of structure formation as possible with as few assumptions as possible, dynamic range limitations nonetheless force them to adopt a number of inputs, a few of which are calibrated empirically. As it is sometimes difficult to keep track of what cosmological simulations predict and what they assume, we here list the inputs into our simulations that we do *not* tune:

- (i) The stellar initial mass function
- (ii) The intrinsic stellar emissivity as a function of wavelength and metallicity
- (iii) The QSO emissivity at 1 Ryd as a function of redshift, the QSO continuum slope, and $f_{\text{esc,QSO}}$

name	RT grid ¹	A^2	$f_{\text{esc,max}}^2$	M_g/M_\odot^3	Γ_{-12}^4	γ/H^5
n256noRT	HM12	–	–	20.5	(0.301)	–
n256RT32	32 ³	1.95	0.36	20.5	0.100	2.44
n256RT64	64 ³	3.4	0.5	20.5	0.385	3.02
n512noRT	HM12	–	–	2.56	(0.301)	–
n512RT64	64 ³	3.45	0.5	2.56	0.272	2.69

Table 1. Our simulations. All have the same initial conditions spanning a cubical volume $12h^{-1}\text{Mpc}$ to a side. ¹Number of grid cells in RT grid; ²cf. Equation 7; ³ Gas particle mass in $10^5 M_\odot$; ⁴ HI photoionization rate at $z = 5.75$ ⁵ Ionizing photons emitted per hydrogen atom when $X_{\text{HI,V}} < 1\%$.

(iv) The metal yield from Type II and Type Ia SNe and from AGB stars

(v) The delay time distribution of Type Ia SNe

(vi) The mass-loading factor $\eta_{\text{W}}(M_*)$ of galactic outflows

In the past, η_{W} was treated as a relatively free parameter with its normalization adjusted to match observations of galaxies and metal absorbers (Oppenheimer & Davé 2008; Oppenheimer et al. 2009). However, we now adopt the Muratov et al. (2015) dependence of η_{W} on M_* , which in turn derives directly from high-resolution simulations. Hence this scaling does not involve free parameters. The following inputs are treated more freely:

(vii) The ionizing escape fraction from galaxies $f_{\text{esc,gal}}$

(viii) The velocity of galactic outflows

(ix) The decoupling and recoupling criteria for outflowing gas

The history of star formation is less sensitive to (viii) than to (vi). For example, in low-resolution simulations, halving the normalization in (vi) increases the stellar mass density at $z = 6$ by a factor of 2.13 whereas halving the normalization in (viii) increases it by a factor of 1.53. Meanwhile, (ix) has almost no effect on it at all (see Schaye et al. 2010 for a more thorough discussion of subgrid parameters in cosmological simulations). Hence *by far the most significant free parameter in our simulation, and the only one that is tuned to match observations in a precise way, is $f_{\text{esc,gal}}$.*

2.6 Table of Simulations

In Table 1, we summarize our simulations. It is critical for reionization simulations to resolve star formation in halos down to the hydrogen cooling limit of roughly $10^8 M_\odot$. Star formation does occur in the abundant population of lower-mass halos, but it is stochastic and inefficient (Wise et al. 2014), and probably does not dominate the overall history of reionization (Ricotti & Ostriker 2004; Greif & Bromm 2006; Ahn et al. 2012; Chen et al. 2017a). Our highest-resolution simulations model $10^8 M_\odot$ halos with roughly 62 dark matter and gas particles. This may fall somewhat short of completely resolving the lowest-mass hydrogen cooling halos, but it is more than sufficient in ionized regions, where the minimum halo mass for efficient gas accretion rapidly grows to $\sim 10^9 M_\odot$ (Okamoto et al. 2008). All of our simulations span the same $12h^{-1}\text{Mpc}$ cubical volume, but they use varying resolutions for the hydrodynamic and radiation transport solvers. Additionally, two simulations have been run with

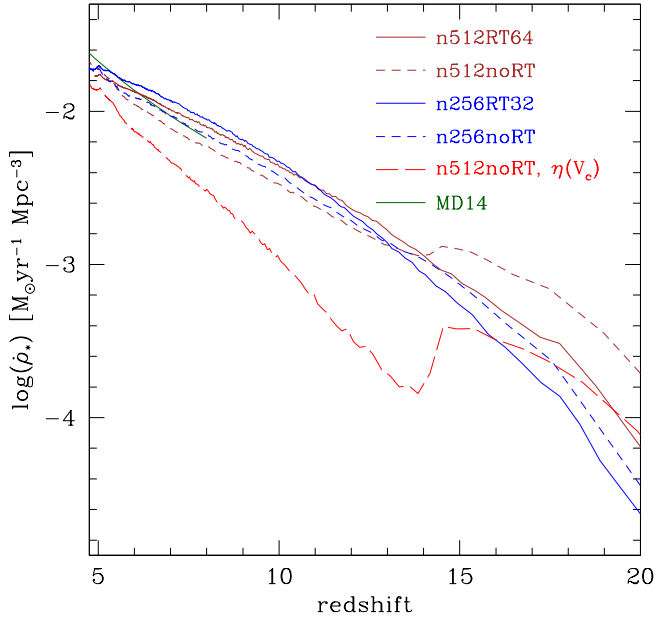


Figure 2. The comoving star formation rate density $\rho_*(z)$ in our simulations as compared to observations (Madau & Dickinson 2014; solid green curve). Simulations that assume the Muratov et al. (2015) mass-loading factor $\eta_{\text{W}}(M_*)$ yield excellent agreement with observations out to $z = 8$, with small differences driven by photoionization heating and resolution.

the Haardt & Madau (2012, HM12) ionizing background for comparison with other works.

The sixth and seventh columns present predictions that show how our simulations compare favorably with observational inferences from the LAF. In particular, the sixth column compares the volume-averaged HI photoionization rate at a fiducial redshift $z = 5.75$; numbers in parentheses indicate the HM12 model. All of our simulations are within a factor of 3 of the HM12 model, with our high-resolution simulation closest of all. The seventh column reports the total number of ionizing photons per hydrogen atom emitted into the IGM (i.e., after $f_{\text{esc,gal}}(z)$ is accounted for) when the volume-averaged neutral hydrogen fraction drops below 1%; this is within the range 2.4–3 that is favored by observations (Bolton & Haehnelt 2007) and the updated analytical model presented by Madau (2017).

3 RESULTS

3.1 Star Formation

In Figure 2, we compare the total simulated star formation rate density ρ_* versus the recent synthesis of available observations by Madau & Dickinson (2014). The simulated ρ_* is computed as the total star formation rate over all gas regardless of the host galaxy’s luminosity. The good agreement between all three solid curves suggests that, broadly, adopting $\eta_{\text{W}}(M_*)$ from Equation 8 of Muratov et al. (2015) leads to excellent agreement with the observationally-inferred trend out to $z = 8$, the highest redshift where observations were

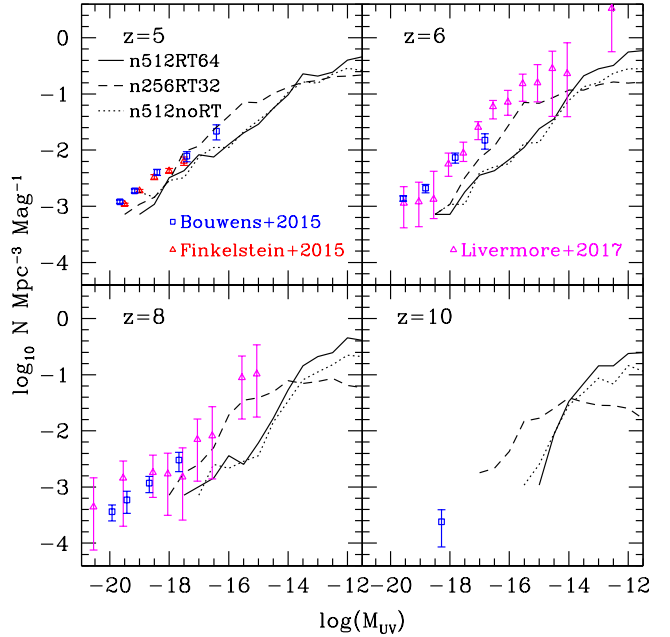


Figure 3. UV luminosity functions at four selected redshifts as compared to observations. At our lower resolution (long-dashed), agreement is sound at all redshifts where measurements and simulations overlap. At higher resolution (solid), the simulation increasingly underproduces observations at $z > 5$ owing to pre-processing of gas in small systems. Re-running the pl12n512 simulation using the HM12 background (dotted) yields almost the same UV LF.

available when this fit was calibrated (see also Davé et al. 2016; Fontanot et al. 2017). By contrast, comparing the red long-dashed and brown short-dashed curves reveals that adopting the dependence $\eta_{\text{W}}(V_c, z)$ on circular velocity and redshift (Equations 4 and 5 of Muratov et al. 2015) leads to drastically oversuppressed star formation at early times (note that it is not surprising that this formulation of η_{W} may be less accurate at early times given that it was calibrated from a small number of simulated halos at $z = 1-3$).

Photoionization heating suppresses star formation in halos less massive than $\sim 10^9 M_\odot$ (Okamoto et al. 2008), leading to the possibility of a rapid dip in ρ_* if the photoionization heating rate jumps (Barkana & Loeb 2000). In simulations that assume the Haardt & Madau (2012) UVB, this occurs at $z = 15$. The effect is amplified by the non-linear coupling between photoionization heating and outflows (Pawlik & Schaye 2009; Finlator et al. 2011), leading to a particularly dramatic drop when very strong winds are modeled at high resolution (red long-dashed curve). Photo-heating begins at earlier times in models that include a more realistic, extended reionization history because the UVB appears as soon as the galaxies do (solid versus short-dashed blue curves). Hence while the predicted amplitude of the dip is sensitive to our assumptions regarding $f_{\text{esc,gal}}$ and galactic outflows, we do not see evidence for it in our most realistic calculation (solid brown curve).

The good agreement between the simulated and observed ρ_* in Figure 2 hides an inconsistency in dynamic range: Whereas the Madau & Dickinson (2014) curve re-

sults from integrating over all luminosities down to $0.03L^*$ ($M_{\text{UV}} \approx -16.4$ at $z \sim 6$), our simulations include (and, at $z \geq 8$, are dominated by) fainter systems while omitting brighter ones owing to volume limitations. A more constraining test is a comparison with the observed UV luminosity function (UV LF). We compute the simulated LFs in a standard fashion: From each snapshot, we extract galaxies using SKID³. Each simulated galaxy consists of hundreds to thousands of star particles, each of which has its own metallicity and age. We compute each star particle’s rest-frame spectrum (in $\text{ergs sec}^{-1} \text{Hz}^{-1}$) using version 2.3 of the Flexible Stellar Population Synthesis library (Conroy et al. 2009), interpolating to its age and metallicity. Each simulated galaxy’s spectrum is then given by a sum over the spectra of its constituent star particles. We multiply synthetic spectra by a factor (0.63/0.67) in order to adjust from a Chabrier (2003) to a Kroupa (2001) IMF (these scaling factors are taken from Section 3.1 of Madau & Dickinson 2014). Finally, we compute the rest-frame 1500\AA luminosity by multiplying the spectrum by an idealized 1500\AA bandpass with a 15% bandwidth and a full width at half-maximum of 225\AA and integrating. We neglect both dust extinction and nebular continuum emission.

In Figure 3, we compare our simulated LFs against recent observations (Bouwens et al. 2015; Finkelstein et al. 2015; Livermore et al. 2017). In the case of our lower-resolution, n256RT32 simulation (dashed), agreement is reasonable throughout $z = 8 \rightarrow 5$. This is a nontrivial success given that the most important parameterized input is $\eta_{\text{W}}(M_*)$, which was in turn *not* empirically-calibrated but rather adopted directly from the high-resolution FIRE simulations (Muratov et al. 2015). At higher resolution (solid), strong winds and efficient star formation in low-mass systems pre-process a great deal of gas at early times. This can clearly be seen in Figure 2 as a boosted overall $\dot{\rho}_*$ at $z > 11$ (compare the solid brown and blue curves). Additionally, more gas condenses into small systems at high resolution, enhancing the faint end of the LF at $z \geq 6$. These effects both reduce the predicted abundance of systems with $M_{\text{UV}} < -14$ in our high-resolution simulation at $z > 5$.

The dotted curve in Figure 3 verifies that ensemble predictions regarding galaxies brighter than $M_{\text{UV}} = -14$ are nearly unchanged if we run our simulations using the HM12 UVB instead of our radiation transport solver. Such galaxies inhabit haloes whose virial temperature exceeds the photoheated IGM’s temperature, hence they are only weakly sensitive to hydrogen reionization.

If the galaxies’ UV luminosities are underproduced at $z > 5$ as suggested by Figure 3, then their stellar masses are also expected to be low. We evaluate whether this is the case in Figure 4, where we compare the predicted stellar mass functions (SMFs) at $z = 5$ and 6 against observations (Duncan et al. 2014; Grazian et al. 2015; Song et al. 2016). The level of agreement is excellent at $z = 5$. At $z = 6$, agreement is good although the SMF normalization may be underproduced by as much as a factor of two. We conclude from Figures 3–4 that our simulations produce roughly the correct number of stars at $z = 5$ but may underproduce them at higher redshifts.

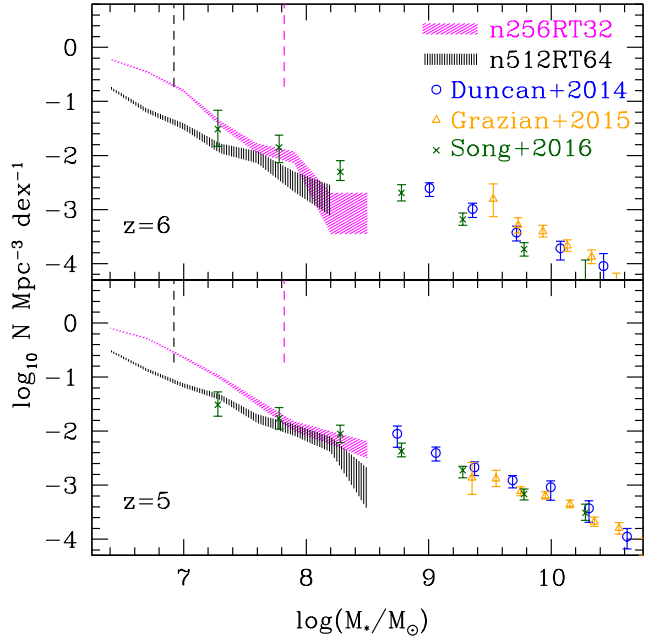


Figure 4. Stellar mass functions at $z = 5$ and 6 in our simulations versus observations. Vertical tickmarks indicate 64-star particle mass resolution limits for our two simulations. While extrapolation from shallower surveys (Duncan et al. 2014; Grazian et al. 2015) suggests that our simulations underproduce stars by up to a factor of four, the deeper Song et al. (2016) measurements are in excellent agreement with the simulations at $z = 5$ and reasonable agreement at $z = 6$.

As in Figure 3, a tendency for the lower-resolution n256RT32 simulation to produce more bright, massive galaxies and fewer faint, low-mass ones is evident. The discrepancy diminishes above its 64-star particle resolution limit of $6.56 \times 10^{10} M_{\odot}$. It occurs because, at the n256RT32 simulation’s resolution, gas first reaches star-forming densities in $\sim 10^9 M_{\odot}$ halos. In the n512RT64 simulation, gas first condenses more realistically into lower-mass galaxies, which in turn may be comparable to the progenitors of the Milky Way dwarf satellites (Finlator et al. 2017). This long tail extending to unobservably low masses is not unique to *Technicolor Dawn*; it is a generic prediction also seen, for example, in the Sherwood Simulations (Keating et al. 2016).

Figures 3–4 indicate that both the SFR and M_* are low for a given halo mass. A simple way to verify that neither of these discrepancies is dominated by observational bias (for example, owing to the shape of the star formation history that is assumed when deriving stellar mass) is to compare the predicted and observed M_* -SFR relationships: if the simulated SFRs are simply oversuppressed, then their integral will be suppressed by the same factor, leaving the ratio intact. We show this comparison at $z \sim 6$ with recent observations (Santini et al. 2017; Salmon et al. 2015) in Figure 5. Note we plot the simulated “current mass” on the x-axis; that is, the mass that remains in long-lived stars. We include only galaxies that contain at least 64 star particles.

The simulated loci overlap well, indicating that the ratio SFR/M_* does not suffer from resolution limitations. Comparing to observations is difficult owing to the poor overlap

³ <http://www-hpcc.astro.washington.edu/tools/skid.html>

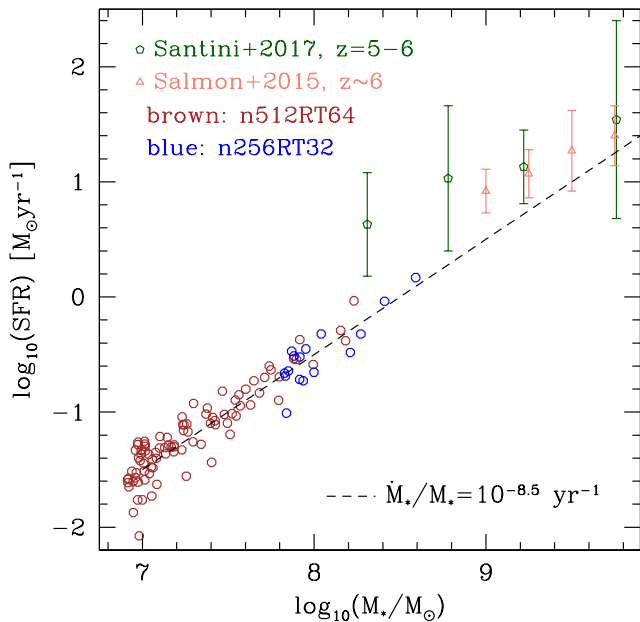


Figure 5. The predicted and observed relations between stellar mass and star formation rate at the end of the reionization epoch. Our simulations predict a constant specific star formation rate of $10^{-8.5}\text{yr}^{-1}$ (dashed line) that is insensitive to resolution limitations. This agrees with the more massive observed systems but underproduces low-mass ones at the 1–1.5 σ level.

in dynamic range, but broadly we find that the predicted SFR is no more than 1–1.5 σ below observations. This is plausible agreement given that photometric techniques may artificially flatten the M_* -SFR relation (Salmon et al. 2015).

In summary, while adopting the Muratov et al. (2015) outflow scalings yields remarkable agreement with the total $\dot{\rho}_*$, the agreement may mask a tradeoff whereby the simulations predict a great deal of star formation in faint galaxies at the expense of the observable population, which are in turn somewhat oversuppressed at $z > 5$. This effect does not necessarily reflect an error in the Muratov et al. (2015) scalings. First, we have adopted only their mass loading factor; our adopted outflow velocities are higher because our low resolution does not treat the launch radius or velocity distribution realistically. Second, the ultimate fate of ejected gas likely depends on the host halo and environment, whereas we tie it exclusively to the stellar mass, potentially permitting overly-efficient outflows. It is easy to imagine explicitly tuning our outflows in order to improve the level of agreement in Figures 2–5; we will return to this in Section 4.2.

3.2 Metal Enrichment

As we have updated our prescriptions for metal enrichment, it is timely to verify that the simulated CGM has a realistic metallicity. The most robust metallicity measurements come from damped Lyman- α absorbers (DLAs), which trace low-ionization gas in conditions where ionization corrections are negligible and metal mass fractions may be measured directly (Rafelski et al. 2012). Recent observations have uncovered DLAs out to redshifts of 4.5–5.5 (Rafelski et al.

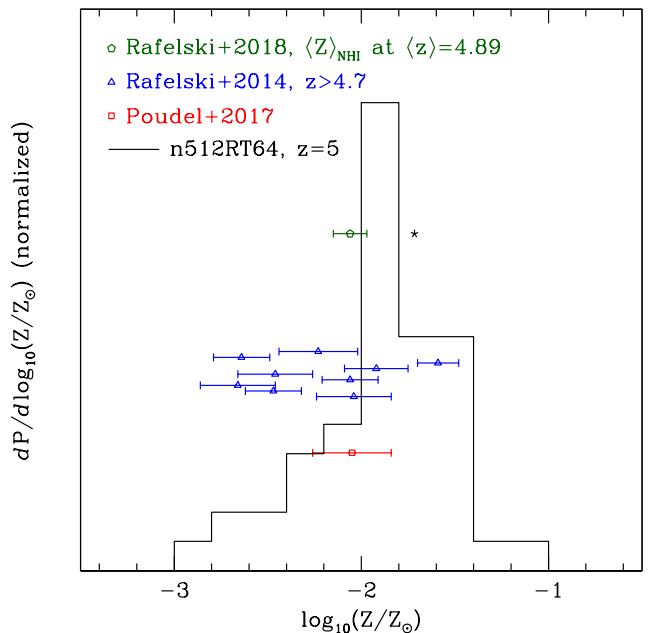


Figure 6. Comparison between the predicted and observed DLA metallicity distributions at $z \sim 5$. The solid histogram gives the predicted probability density normalized to unit area and displayed with a linear y-axis. Squares and triangles represent observed DLA metallicities at $z > 4.7$, offset arbitrarily on the y-axis for visibility. The green pentagon and black star represent N_{HI} -weighted mean metallicities from an observed sample at $\langle z \rangle = 4.89$ (Rafelski 2018, private communication) and the simulation at $z = 5$, respectively. There is good overlap between the observed and predicted metallicity ranges although the simulation may be biased high.

2012, 2014; Poudel et al. 2018). We now compare these measurements directly to our n512RT64 simulation at $z = 5$.

We identify simulated DLAs by searching for regions along simulated sightlines where the total HI column density $\log(N_{\text{HI}}/\text{cm}^{-2})$ within a 200 km s^{-1} segment exceeds 20.2. This returns $dN = 49$ DLAs over an absorption path length⁴ of $dX = 351.01$. The implied number density of $dN/dX = 0.14$ is consistent with the 68% confidence range of 0.0638–0.1435 recently measured at $z = 4.83$ –5.00 (Bird et al. 2017, Table A6). We then compute each simulated DLA’s metallicity as the HI-weighted average of the summed mass fraction in C, O, Si, and Mg within each pixel. We normalize to solar by assuming a total solar mass fraction of 0.00958 for these elements (Asplund et al. 2009). The distribution of simulated DLA metallicities computed in this way is displayed as a normalized histogram in Figure 6. It spans over two orders of magnitude, with an HI-column weighted mean of -1.72 (five-pointed star).

To test this predicted distribution, we use observed metallicities of HI-selected systems with $\log(N_{\text{HI}}) \geq 20.2$ as

⁴ The “absorption path length” $dX \equiv (1+z)^2 H_0/H(z) dz$ is used to quantify the density of absorbers along a sightline in a way that factors out cosmological expansion (Bahcall & Peebles 1969): for a non-evolving population, the number of objects per absorption path length dN/dX does not vary with redshift.

$z > 4.7$; these are shown as blue and red colored points with errors (the positions of observed systems on the y-axis is arbitrary). For the Poudel et al. (2018) system at $z = 4.829$, we adopt the oxygen metallicity, whereas for the Rafelski et al. (2014) systems we adopt the bulk metallicity from the final column of their Table 1. For the present, we neglect differences between the particular metal species that are used because the resulting metallicities, when normalized to solar, generally agree within 1σ .

There is broad agreement between the simulated and observed DLA metallicity ranges. In detail, however, the simulations may overproduce the CGM metallicity: Computing the HI-weighted mean metallicity of a sample of high-redshift DLAs with a mean redshift $\langle z \rangle = 4.89$ yields a mean metallicity normalized to solar of $\log(Z/Z_{\odot}) = -2.06 \pm 0.09$ (green pentagon; Rafelski 2018, private communication) whereas our simulation predicts -1.72 in the same units (black five-pointed star). A similar discrepancy of -2.06 (observed) versus -1.86 (simulated) is obtained when the median simulated metallicities at $z = 5$ are compared with the median observed metallicities of DLAs at $z > 4.7$ from Rafelski et al. (2014) and Poudel et al. (2018), so the effect is robust to the choice of statistic.

The existence and sense of this offset are likely robust to systematic uncertainties for several reasons. First, observations suggest that metal-poor DLAs are generally α -enhanced (Cooke et al. 2011). If true, and if the observed metallicities are weighted towards α -elements, then correcting for this could push the total observed metallicities down. Second, our fiducial n512RT64 simulation underproduces stars—and therefore metals—at early times (Figure 3). Although the effect is weak by $z < 6$, correcting for it would increase the predicted metallicities. Finally, the simulated UVB may be too weak at $z < 6$ (Section 3.3). Qualitatively, this will bring overly-rarified and presumably underenriched CGM gas into the simulated DLA sample; correcting for it would reduce the predicted DLA number density and increase their metallicities.

It will be important to confirm whether the factor-of-two offset survives when these details are taken into account and the observed sample is larger. If so, then it suggests the need for lower metal yields (perhaps by reducing the hypernova fraction; Section 2) or stronger feedback at earlier times. Given that DLA metallicities span two orders of magnitude, however, and given that the simulations were in no wise calibrated against this observation, the preliminary agreement in Figure 6 is unexpectedly good.

3.3 The History of Hydrogen Reionization

A central goal of our development efforts involves using our star formation and radiation transport model to generate a realistic reionization history. It is of obvious interest to verify that our model does so. In order to build intuition regarding the role of faint galaxies in driving hydrogen reionization, we map in Figure 7 the spatial relationship between galaxies and HII regions at $z = 7.5$ in our high-resolution simulation. At this redshift, the volume-averaged neutral hydrogen fraction $X_{\text{H I, V}}$ is 33%. The color bar codes for the HI column density through a slice of simulation 49 km s^{-1} thick and $12h^{-1}\text{Mpc}$ to a side. The overlap of HII regions is well underway in this snapshot. On the left and right sides

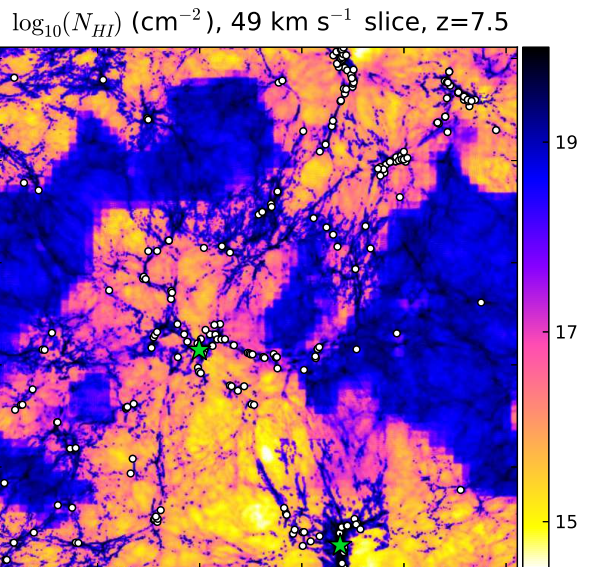


Figure 7. The HI column density through a 49 km s^{-1} slice at $z = 7.5$, when the predicted neutral hydrogen volume fraction is 33%. The side length is $12h^{-1}\text{Mpc}$ comoving Mpc, or 2.08 proper Mpc at this redshift. Points and stars indicate the positions of galaxies that are fainter and brighter than $M_{\text{UV}} = -15$, respectively. Large-scale ionized regions are threaded by dense filaments, which clearly trace the positions of faint galaxies. Note that the slightly pixelated appearance of the ionization fronts reflects the finite resolution of our radiation transport solver, which is coarser than the hydrodynamic solver.

there remain Mpc-scale regions that are both partially-to-completely neutral and devoid of galaxies. Between the neutral regions lie several HII regions that are about to merge. These are threaded by filamentary Lyman-limit systems of dense, still-neutral gas that host the galaxies, which are indicated by white dots or green stars. Only two of these galaxies are observable ($M_{\text{UV}} < -15$), reinforcing that, in the standard galaxy-driven reionization scenario, most of the activity is in very faint systems. The ratio of the volume-averaged and mass-averaged neutral hydrogen fractions at this redshift is $X_{\text{H I, V}}/X_{\text{H I, M}} = 0.87$, indicating that the voids are more ionized than the filaments. In other words, the reionization topology is at this point “outside-in”, the precursor to the final stage where the filaments are all that remain neutral (Finlator et al. 2009).

Turning from the qualitative to the quantitative, we have insured a realistic reionization history by calibrating our two-parameter model for $f_{\text{esc, gal}}(z)$ to match simultaneously observations of the optical depth to Thomson scattering τ_{es} and the inferred total ionizing photon production rate at $z = 5$ (this is in fact our *only* empirical calibration). In Figure 8, we confirm that this calibration yields a volume-averaged HI fraction that passes below 50% at $z \sim 8-8.5$ and reaches 1% around $z \sim 6$ (top panel). The corresponding predicted integrated optical depths to Thomson scattering are 0.05463 and 0.06048 for the low- (dashed) and high-resolution (solid) simulations, respectively, both in excellent agreement with the observed range of 0.058 ± 0.012 (Planck Collaboration et al. 2016b). Given that we have independently calibrated $f_{\text{esc, gal}}$ for these two

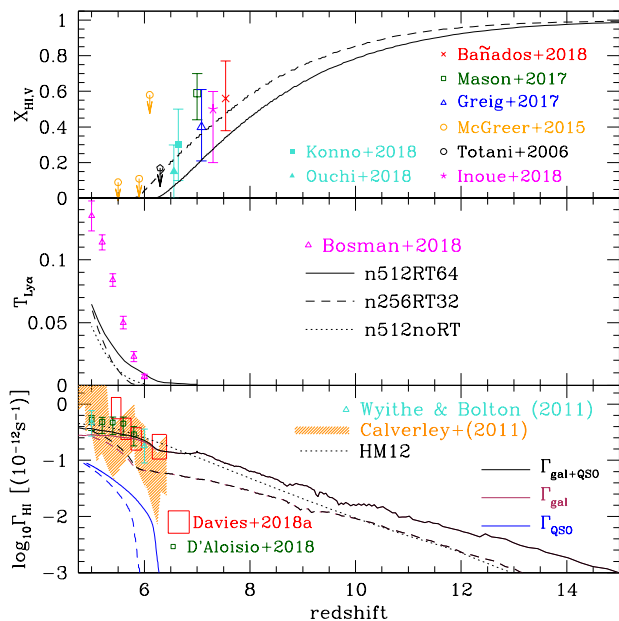


Figure 8. *Top:* Volume-averaged neutral fraction as a function of redshift. Observations: The equivalent widths of Lyman Alpha Emitters (LAEs) (green square; magenta star: Mason et al. 2018; Inoue et al. 2018); LAE luminosity function (turquoise square Konno et al. 2018) and clustering (turquoise triangle: Ouchi et al. 2018); the damping wing of a QSO at $z = 7.09$ (blue triangle, Greig et al. 2017) and $z = 7.54$ (red cross, Bañados et al. 2018); the Lyman- α and Lyman- β dark pixel fractions (orange circles, McGreer et al. 2015); and a GRB damping wing (black pentagon, Totani et al. 2006). *Middle:* Mean transmitted flux fraction in the Lyman- α forest versus observations (Bosman et al. 2018). *Bottom:* Volume-averaged HI photoionization rate compared with observations. All plotted uncertainties are 1σ .

resolutions, this is not a demonstration of resolution convergence. Instead, it shows that some of the lack of convergence associated with incompletely modeling radiation transport on small scales can be compensated for by allowing $f_{\text{esc,gal}}$ to vary.

Our simulated hydrogen reionization histories are consistent with the strong upper limits on $X_{\text{HI},V}$ derived from the dark pixel fraction in the Lyman- α and Lyman- β forests of high-redshift quasars (circles) as well as the inferred upper limit from the damping wing of GRB 050904 (pentagon). They are in agreement with the neutral fraction inferred from the damping wing of QSOs at $z = 7.09$ (blue triangle) and at $z = 7.54$ (red cross), although both of these prefer the somewhat later reionization history of our n256RT32 simulation. We do not show the recent re-analysis of the $z > 7$ QSO damping wings by Davies et al. (2018a), but we note that, while it yields $X_{\text{HI},V}$ values that are consistent with previous work, they are slightly higher overall, again favoring our n256RT32 simulation. Our simulated $X_{\text{HI},V}$ are $1.5\text{--}2\sigma$ low compared to inferences based on the observed Lyman- α equivalent width distribution of Lyman break galaxies by Mason et al. (2018, square), but in agreement with the complementary analysis by Inoue et al. (2018, 5-pointed star), emphasizing the challenging nature of this measurement. They are also consistent with inferences

from clustering of Lyman- α emitters (Ouchi et al. 2018) and their luminosity function (Konno et al. 2018). Overall, we conclude that both of our simulations yield broadly realistic reionization histories although current observations may show a slight systematic preference for the slower reionization history of our n256RT32 simulation.

An even more demanding test of our model than the reionization history is the nature of the post-reionization UVB, which is well-measured from observations of the LAF. In the middle panel of Figure 8, we compare the mean transmission at the Lyman- α edge predicted from our simulations $T_{\text{Ly}\alpha}$ versus observations by Bosman et al. (2018). We compute the predicted transmission by simply averaging over simulated Lyman- α spectra at each redshift. For both radiation transfer simulations, the predicted transmission begins rising at roughly the correct redshift, but it grows more slowly than observations indicate. If we adopt the HM12 UVB (n512noRT; dotted curve), then the mean transmission is likewise underproduced.

We do not believe that resolution limitations are the primary source of this discrepancy. Bolton & Becker (2009) have shown that the underdensities that dominate Lyman- α transmission at $z \geq 5$ are rare and small, requiring both large volumes and high resolution. They suggest that, at our mass resolution and volume (see the green curve in their Figure 1), the mean Lyman- α transmission is only marginally resolved and biased somewhat low at $z = 5$. We have repeated their experiment by running simulations with a spatially-homogeneous HM12 UVB down to $z = 5$ in volumes spanning 6, 12, and 18 $h^{-1}\text{Mpc}$, each with a gas particle mass of $2.56 \times 10^5 M_{\odot}$. At $z = 6$, the transmissions are (0.0012, 0.0015, 0.0013). At $z = 5$, they are (0.042, 0.047, 0.046). Likewise, increasing the gas particle mass within the $12h^{-1}\text{Mpc}$ volume by a factor of 8 (i.e., using 2×256^3 instead of 2×512^3 particles) reduces the transmission at $z = 5$ from 0.047 to 0.042. These experiments suggest that, over the (limited) range of volumes and resolutions that we consider, we expect no more than a $\sim 10\%$ impact of resolution limitations on the mean transmission.

Our results are supported by Oñorbe et al. (2017), who recently performed a resolution convergence study of the LAF at $z = 5\text{--}6$ in simulations that assume an optically-thin UVB. Their findings imply that the mean transmission in our n512RT64 simulation may be biased low by $\sim 5\%$ owing to mass resolution limitations while being biased high at the $\sim <1\%$ level owing to limited simulation volume. Likewise, the tests reported in Appendix A of D’Aloisio et al. (2018) indicate that our simulated mean transmission is converged to 10% with respect to resolution.

We speculate that, instead, the UVB may be strengthening too slowly in our simulations despite the agreement in the UVB amplitude (bottom panel), reflecting either uncertainty in $f_{\text{esc,gal}}(z)$ or systematic error in the observed UVB amplitude. Our inability to reproduce the rapid evolution in the observed mean transmission even when effects such as UVB fluctuations and scatter in the $\rho - T$ distribution (Figure 13) are treated accurately echoes the findings of Bosman et al. (2018), and seems to be a generic problem afflicting cosmological simulations in which the adopted UVB amplitude matches observations.

Our results also echo superficially those of Gnedin et al. (2017), who performed a detailed comparison between the

predicted statistical properties of the LAF from the path-breaking CROCS simulation suite versus observations. They also found that their simulations yielded an IGM that was somewhat too opaque (as quantified by the widths of Lyman- α transmission peaks), though likely for very different reasons. While their spatial resolution is comparable to ours (≤ 100 physical parsecs at all $z > 6$), their simulation boxes are 2–3.3 \times as wide and their predicted reionization history ends at $z \sim 7$; both of these effects could boost the predicted mean transmission with respect to ours. They concluded that the source of the discrepancy was unclear, although proximity zones around foreground quasars were one possible unaccounted-for issue. To the extent that this is true, we should expect our simulations to have the same problem.

In the bottom panel, we compare the predicted and observed volume-averaged hydrogen photoionization rate Γ_{HI} and its contributions from galaxies and quasars. Quasars contribute only \sim a few % of the hydrogen-ionization photons at $z > 5$, consistent with the consensus that is emerging in the literature (Finlator et al. 2016; D’Aloisio et al. 2017; Parsa et al. 2018; Qin et al. 2017; Hassan et al. 2018; McGreer et al. 2018). For both simulations, $\Gamma_{HI} = 0.1\text{--}0.5 \times 10^{-12} \text{s}^{-1}$ at $z \geq 5$, in excellent agreement with most observations (Calverley et al. 2011; Wyithe & Bolton 2011; Davies et al. 2018b; D’Aloisio et al. 2018). In particular, the most recent measurements of the post-reionization photoionization rate (Davies et al. 2018b; D’Aloisio et al. 2018) seem clearly to prefer the n512RT64 model, which in turn closely tracks the Haardt & Madau (2012) model. None of the models reproduce the sharp decline in Γ_{HI} from $z = 5.5 \rightarrow 6$ deduced by Davies et al. (2018b). Given that the Davies et al. (2018b) measurements are presented as a proof-of-concept based on a single sightline, and given that D’Aloisio et al. (2018) do not recover this jump, it is not clear whether this behavior is real.

In summary, the comparisons in Figure 8 show that, maugre dynamic range limitations and lingering uncertainty regarding $f_{\text{esc,gal}}(z)$, our simulations yield a reionization history *and* an early UVB evolution that are in encouraging agreement with observations. However, we find interesting tensions between the implications of the different observations: Whereas observations of $X_{\text{HI,IV}}$ tend to prefer the slower reionization history of our n256RT32 simulation, observations of Γ_{HI} prefer the more intense ionizing background of our n512RT64 simulation. Meanwhile, both simulations yield a mean transmission in the LAF that is low compared to observations. This is also true of the HM12 simulation, whose predicted mean transmission tracks the n256RT32 simulation even though its Γ_{HI} tracks the n512RT64 simulation. We will show below that the HM12 UVB and, perhaps more importantly, the assumption of ionization equilibrium, leads to a colder IGM at $z < 6$ (see also Puchwein et al. 2015 and Figure 13), which undoubtedly contributes to its lower transmission.

3.4 The Simulated UVB

As the normalization, slope, and spatial fluctuations in the reionization-epoch UVB remain a major source of uncertainty in large-scale models of reionization, it is of interest to study how it evolves and to compare it with complementary models. In Figure 9, we show the UVB predicted

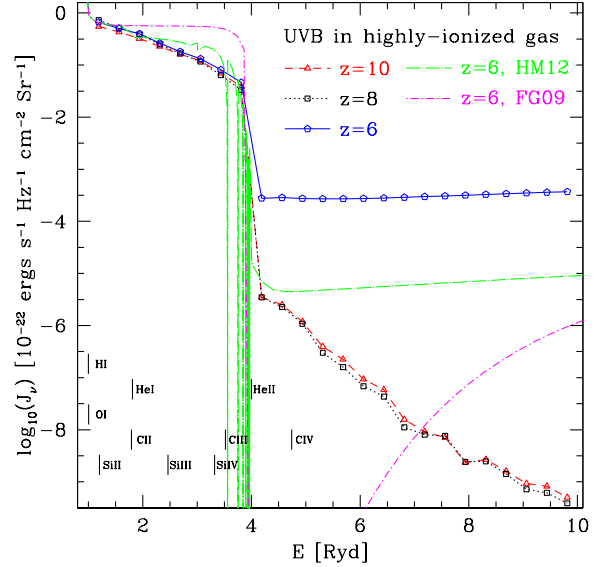


Figure 9. The volume-averaged mean UVB in voxels where the HI neutral fraction is less than 0.5% at three representative redshifts. The galaxy contribution to the UVB in ionized regions is nearly redshift-independent, while the quasar contribution dominates above 4 Ryd after $z = 8$. The UVBs predicted by Haardt & Madau (2012) and Faucher-Giguère et al. (2009) at $z = 6$ are included for comparison (long dash-dotted green and short dash-dotted magenta, respectively). The ionization potentials of common high-redshift CGM ions are indicated at the bottom of the figure.

by our n512RT64 simulation in highly-ionized regions (local $X_{\text{HI,IV}} < 0.005$) at three representative reionization-epoch redshifts. Remarkably, it is invariant at $z > 6$ between the HI and He II ionization edges. At higher energies, the UVB is dominated by galaxies prior to $z = 8$ and quasars afterwards.

Comparing our simulated UVB with two complementary models reveals weak disagreement for $h\nu < 4$ Ryd and dramatic disagreement at higher energies. The HM12 model (long dash-dotted green) is in good agreement with *Technicolor Dawn* below 4 Ryd although its inclusion of bound-bound He II transitions leads to sharp absorption features between 3–4 Ryd. By contrast, it predicts a He II-ionizing background that is $\approx 30\times$ weaker. Meanwhile, the Faucher-Giguère et al. (2009) background (dash-dotted magenta)⁵ has a bluer spectral slope below 4 Ryd and is much weaker than the other models at higher energies. From this figure alone, it is easy to see that the expected CIV fraction in the CGM remains subject to much larger systematic uncertainty than, for example, Si IV owing to lack of theoretical understanding of the early stages of He II reionization. Put differently, this re-iterates that CIV offers unique insight into the early stages of He II reionization just as O I tracks the early stages of HI reionization (Oh 2002; Keating et al. 2014).

An additional strength of the *Technicolor Dawn* simulations is their ability to capture spectral filtering of the UVB by the IGM. This effect is potentially important as it gives

⁵ <http://galaxies.northwestern.edu/uvb/>

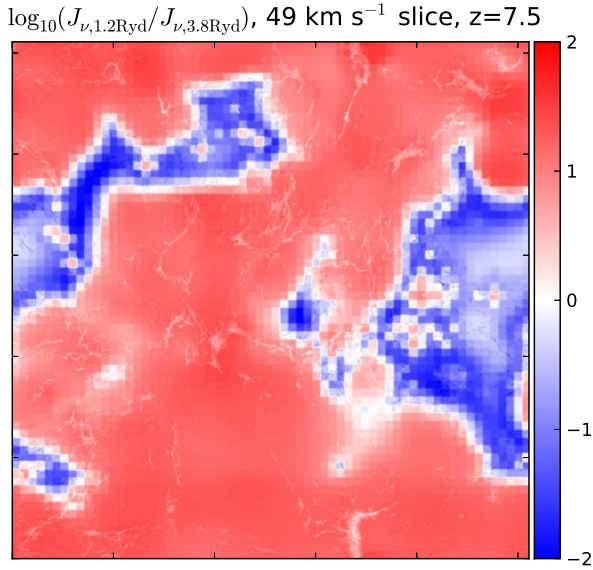


Figure 10. The UVB’s spectral hardness as measured by the ratio of the mean specific intensities J_ν in energy bins centered at 1.1875 and 3.8125 Ryd in the same slice as in Figure 7. Blue and red regions have blue and red spectral slopes between 1–4 Ryd, respectively. The impact of spectral filtering is clearly seen both in HI regions and in self-shielded filaments.

rise to small-scale fluctuations in the UVB’s spectral hardness, which impacts the IGM’s ρ – T relation as well as metal absorber characteristics. We demonstrate that our simulations account for spectral filtering in Figure 10, which maps the ratio of the UVB strength J_ν in frequency bins centered at 1.1875 and 3.8125 Ryd. In reionized regions, J_ν is flat (white) or declines with energy (red), whereas in filaments and neutral regions it increases (blue). Importantly, the effect is accounted for both by the radiation transport solver itself and by the subgrid self-shielding prescription, which is frequency-dependent and preferentially shields dense regions from softer photons.

3.5 The IGM Temperature

How hot is the reionization-epoch IGM? Its temperature sources a factor-of-two uncertainty in reionization calculations owing to the temperature dependence of the recombination rate: colder gas recombines faster, consuming more photons, whereas hotter gas requires fewer photons and a generally harder ionizing continuum. Additionally, the reionized IGM’s cooling time is longer than its recombination time, leading to long-lived “footprints” of inhomogeneous reionization in the form of temperature fluctuations that source extra inhomogeneity in the IGM opacity and suppress small-scale fluctuations in the Lyman- α forest flux power spectrum (Section 3.6; D’Aloisio et al. 2015; Keating et al. 2018). A key advantage to using our multifrequency, on-the-fly radiation transport solver is that the IGM temperature evolution and its spectral filtering impact on the UVB are faithfully modeled.

The maximum temperature of post-reionization gas may be estimated from the UVB as the mean heat deposited per photoelectron divided by the total number of particles

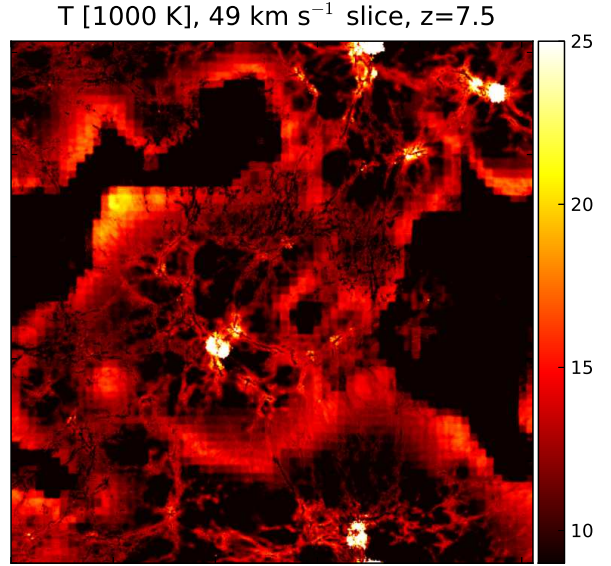


Figure 11. The mass-weighted mean gas temperature through the same slice as in Figure 7. Gas is heated by ionization fronts as well as in dense regions near star-forming galaxies where adiabatic compression and outflows are in play.

per photoelectron in reionized gas. In the optically-thin approximation, the photoionization heating rates for hydrogen and helium are

$$\mathcal{H}_{\text{HI}} = n_{\text{HI}} \int dv \frac{4\pi J_\nu}{hv} \sigma_{\nu,\text{HI}} h(v - \nu_{i,\text{HI}}) \quad (9)$$

$$\mathcal{H}_{\text{HeI}} = n_{\text{HeI}} \int dv \frac{4\pi J_\nu}{hv} \sigma_{\nu,\text{HeI}} h(v - \nu_{i,\text{HeI}}) \quad (10)$$

Likewise, the photonization rates are

$$\Gamma_{\text{HI}} = n_{\text{HI}} \int dv \frac{4\pi J_\nu}{hv} \sigma_{\nu,\text{HI}} \quad (11)$$

$$\Gamma_{\text{HeI}} = n_{\text{HeI}} \int dv \frac{4\pi J_\nu}{hv} \sigma_{\nu,\text{HeI}} \quad (12)$$

The maximum post-reionization temperature is then

$$\frac{3}{2} k_B \Delta T = \frac{1}{2} \frac{\mathcal{H}_{\text{HI}} + \mathcal{H}_{\text{HeI}}}{\Gamma_{\text{HI}} + \Gamma_{\text{HeI}}}, \quad (13)$$

where the leading factor of 1/2 on the right-hand side accounts for the fact that there are twice as many particles as electrons in ionized gas. Applying this to the simulated UVBs in Figure 9 leads to $\Delta T = 18,000$ – $19,000$ K, depending on the redshift. This corresponds to mean photon energies of 18.3–18.6 eV, consistent with the range that is required in order to match observations of the post-reionization IGM temperature (Keating et al. 2018). Photoionization of He I increases the heating rate by 6–7% and the ionization rate (that is, total photoelectron production rate) by 5–6%. This level of heating is significantly less than what is required to reproduce the observed distribution of optical depths in the LAF (30,000 K; D’Aloisio et al. 2015). Moreover, gas in and behind ionization fronts cools efficiently owing to bound-bound transitions and Compton cooling (McQuinn 2016), so recently-reionized gas will generally be even cooler. Quantifying this effect is nontrivial, but a crude investigation of our ρ – T diagrams from $z = 11$ – 6 (not shown) reveals maximal post-reionization temperatures rising smoothly from

14,000K at $z = 11$ to 19,000K at $z = 6$, indicating slightly more efficient cooling at higher redshifts as has previously been noted (Keating et al. 2018). In short, our multifrequency UVB is inconsistent with post-reionization IGM temperatures above 20,000 K, and when cooling is taken account, even lower temperatures may be more realistic.

While our simulations do not directly predict post-reionization IGM temperatures above 20,000 K, for completeness, we note that two resolution limitations impact the predicted heating rate within ionization fronts. First, our radiation transport solver’s finite *spatial* resolution smears out ionization fronts, causing gas to spend too much time in a partially-ionized state where collisional excitation cooling is effective. Avoiding this problem requires a spatial resolution that is several times smaller than the size of ionization fronts. For photons with energies $h\nu = 1\text{--}4$ Ryd, the mean free path at mean density in a neutral IGM at $z = 6$ is 5.5–133 comoving kpc, as compared to our simulation’s 277 kpc. Resolution limitations are less severe at higher energies and in voids, which in fact dominate the LAF for $z > 5$ (Bolton & Becker 2009). Nonetheless, our simulations may suffer from over-cooling.

The second way in which our heating rate may be un-converged relates to our finite *energy* resolution. Our heating module assumes that all of the photons within a particular energy bin have an energy corresponding to the middle of that bin. This may lead to overheating or underheating depending on the local spectral slope. By computing the heating owing to a trial UVB that has a fiducial ν^{-2} spectral slope from 1–4 Ryd using increasingly finer energy sampling, we estimate that the post-reionization temperatures with energy bins spaced 0.375 Ryd apart may be up to 23% high in the ionized IGM (where Equations 9–13 apply) and up to 4% low within ionization fronts (where nearly all photons are locally-absorbed).

Equation 13 is idealized in that it applies to an optically-thin medium and ignores cooling. In order to explore how heating proceeds when these effects are accounted for in an inhomogeneous reionization scenario, we show in Figure 11 that the reionized IGM at $z = 7.5$ is indeed heated to 15,000–20,000 K, with the hottest diffuse regions located immediately behind ionization fronts. In fact, comparison of Figures 7 and 11 indicates that heating (correctly) precedes reionization owing to the somewhat longer mean free path of high-energy photons. Isolated areas roughly ~ 100 kpc across can be seen at the top and bottom where the gas is shock-heated to much higher temperatures by galactic outflows. Surrounding these star-forming regions are “webs” of filaments and voids where ongoing reionization is heating the filaments while the voids have already cooled. Meanwhile, outside of HII regions and within self-shielded filaments, the gas is characteristically colder than 10^4 K.

3.6 The Lyman- α Flux Power Spectrum

The middle panel of Figure 8 suggests that the mean transmission in the LAF is reasonable near $z \sim 6$ but then rises too slowly with time. However, this conclusion is quite sensitive to the way in which the continuum level of the observed LAF is inferred. A complementary statistic that is sensitive to reionization while circumventing uncertainty in continuum corrections is the Lyman- α flux power spectrum (for exam-

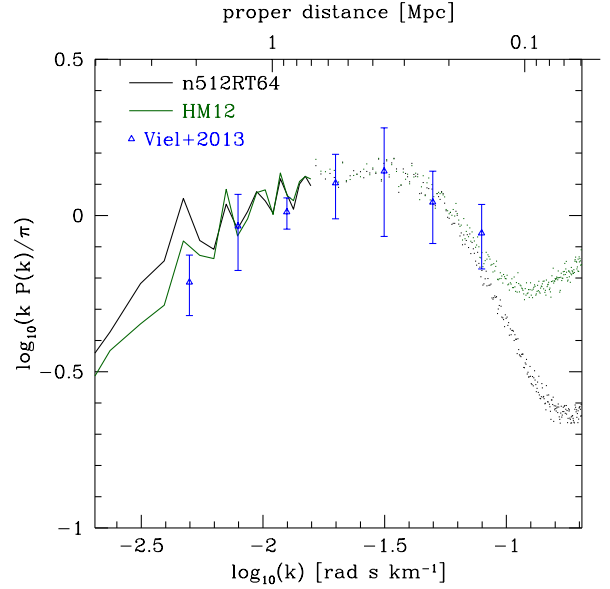


Figure 12. The Lyman- α flux power spectrum at $z = 5.375$ as compared to observations at $z = 5.4$ (Viel et al. 2013a). Black and green points and curves show the simulated flux power spectra for our radiation transport and HM12 models, respectively, after rescaling to the observed mean transmission (see text). The top axis maps wavenumber to proper distance (Mpc). The simulation volume’s proper side length L_p at $z = 5.4$ corresponds to a wavenumber $\log[2\pi/(H(z)L_p)] = -2.4$, which is comparable to the largest measured scale.

ple, Oñorbe et al. 2017). We compute the simulated power spectra in a way that mimics observations: First, we rescale the simulated optical depth at each pixel by a constant factor so that the normalized mean transmission (including pixels where it is negative owing to our error model) matches the continuum-corrected mean flux $\exp(-\tau_{\text{eff}})$. Simulated fluxes that are negative are rescaled in the same way. For consistency with Viel et al. (2013a), we choose $\tau_{\text{eff}}(z = 5.4) = 2.64$. For our n512RT64 and n512noRT simulations, matching this requires us to rescale all optical depths by factors of 0.56 and 0.41, respectively, consistent with the result that the n512RT64 simulation yields a slightly higher mean transmission. The simulated volume-averaged hydrogen photoionization rates at $z = 5.375$ are $3.21 \times 10^{-13} \text{s}^{-1}$ and $3.78 \times 10^{-13} \text{s}^{-1}$ for the n512RT64 and HM12 UVBs, respectively, so interpreting these rescaling factors purely as a modification to the UVB amplitude yields “measurements” of Γ_{HI} at $z = 5.375$ of $5.73 \times 10^{-13} \text{s}^{-1}$ and $9.22 \times 10^{-13} \text{s}^{-1}$. The nearly factor-of-two difference between these inferences reflects the systematically hotter IGM in the *Technicolor Dawn* simulations (Figure 13) and re-iterates that measuring the UVB amplitude from the observed mean transmission in this way is model-dependent (Gnedin & Hamilton 2002).

Having normalized our simulated LAF spectrum, we break it up into chunks of length 8000 km s^{-1} . We then extract the dimensionless power spectrum at each wavenumber k from each chunk following Lukić et al. (2015, Equation 12). Finally, we average in bins of k .

We compare the predicted Lyman- α flux power spectra with observations at $z = 5.4$ by Viel et al. (2013a) in Figure 12. As long as they are rescaled to a common mean

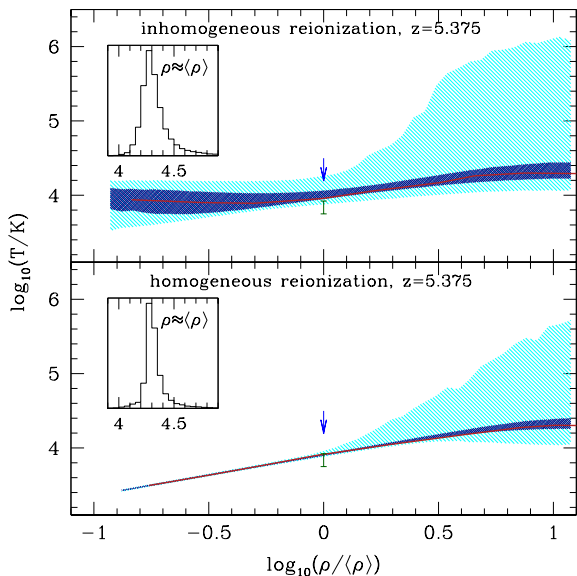


Figure 13. The predicted relationship between temperature and density for underdense to mildly-overdense gas at $z = 5.375$ in our n512RT64 (top) and n512noRT (bottom) simulations. The red curve represents a running median T at fixed ρ while the inner and outer hashed regions enclose 68% and 99% of gas at each density. The green point and blue limit at the mean density from Viel et al. (2013a) and Garzilli et al. (2017), respectively. Inset panels show the normalized distribution of $\log(T/K)$ at the mean density (see text).

transmission, both our n512RT64 and n512noRT simulations predict similar power spectra over the observed range. Moreover, they are within 1σ of observations at all scales. In detail, the n512noRT model (which assumes a spatially-uniform HM12 UVB) predicts significantly more power at very small scales ($k > 0.06 \text{ rad s km}^{-1}$). At the largest observed scale ($k < 0.01 \text{ rad s km}^{-1}$), the RT model predicts somewhat more power owing presumably to residual large-scale fluctuations in the UVB.⁶ It is worth noting that, whereas Viel et al. (2013a) allowed the mean transmission in their simulated spectra to vary about the observed value (from their Equation 4) in order to improve the fit with the observed power spectrum (with a best fit at $z = 5.4$ of 3.09; see their Table II), we find reasonable agreement with the directly-observed optical depth.

What causes the dramatic suppression of small-scale power ($k > 0.1 \text{ rad s km}^{-1}$) in our reionization simulations? It could reflect either a reionization history that begins earlier, yielding increased pressure smoothing, or one that has heated the IGM more efficiently or recently, yielding increased Doppler broadening (Oñorbe et al. 2017). As our radiation transport simulations reionize later than the

⁶ The impact of UVB fluctuations in our model is small compared to the “fluctuating UVB model” in Viel et al. (2013a, Figure 16) for two reasons. First, our galaxy-dominated UVB is generally more homogeneous than their QSO-dominated case. Second, our model includes both temperature and UVB amplitude fluctuations, which tend to have opposing effects on the Lyman- α transmission (Davies et al. 2017, Figure 6).

HM12 UVB (cf. HM12, figure 14), the IGM temperature is the most likely culprit. To emphasize this point, we compare in Figure 13 the predicted relationship between temperature and density for underdense to mildly-overdense gas at $z = 5.375$ in our n512RT64 (top) and n512noRT (bottom) simulations. The only difference between these two simulations is the reionization history: the top panel reflects a mostly galaxy-driven, inhomogeneous reionization scenario that is only 50% complete at $z = 8$ and includes nonequilibrium ionizations and self-shielding. By contrast, the bottom panel reflects the spatially-homogeneous HM12 UVB, which heats the gas significantly already at $z = 15$, and the assumption of ionization equilibrium. Without an inhomogeneous reionization history, we reproduce the well-known power-law ρ - T relation (Hui & Gnedin 1997) by $z = 5.375$. By contrast, our inhomogeneous reionization model sources significant scatter in T at fixed ρ at the same redshift, yielding a slightly “inverted” ρ - T relation, as expected in the immediate aftermath of reionization (for example, Trac et al. 2008; Furlanetto & Oh 2009).

The data points at the mean density indicate that our simulations are consistent with available measurements. Both are below the $1\text{-}\sigma$ upper limit of Garzilli et al. (2017, blue arrow). Possibly more constraining is the green data point, which represents the inferred temperature at the mean density at $z = 5.378$ from Viel et al. (2013a, Figure 10). This measurement, while marginally consistent with both simulations, is systematically lower. The discrepancy may reflect differences in the underlying simulation methodology such as the assumption that gas is in ionization equilibrium with a uniform UVB or the efficiency of photoionization heating. Differences in the reionization history itself are also likely to contribute. For example, their modeling prefers an instantaneous hydrogen reionization redshift of $z = 11.2$ whereas our radiation transport model reaches a 50% neutral fraction around $z \sim 8$. Another difference involves the uncertain timing of He II reionization, the initial stages of which likely boost the temperature scatter in our radiation transport simulation over models in which the UVB first hardens at a lower redshift (McQuinn et al. 2009). Finally, differences in the choice of atomic cooling rates can lead to a $\sim 10\%$ difference in $T(\langle\rho\rangle)$ (Lukić et al. 2015), although any correction to a cooler IGM would only exacerbate the discrepancy with the observed mean transmission. Given these differences, the marginal agreement is, if anything, surprisingly encouraging.

This impact of reionization on the $\rho - T$ relation is strongly density-dependent. The inset panels of Figure 13 show the predicted temperature distribution in each model for gas near the mean density ($0.95 < \rho/\langle\rho\rangle < 1.05$). The median temperatures are quite similar, but the scatter about this median is larger in the case of inhomogeneous reionization. The median temperature and scatter grow systematically to lower overdensities, which may play a larger role in shaping the LAF at $z > 5$ (Bolton & Becker 2009).

The boosted $\rho - T$ scatter is likely complemented by slight adjustments to the gas density distribution owing to the fact that regions that reionized and were pressurized earlier have longer to relax hydrodynamically. Together, these effects erase the tight relationship between overdensity and transmission that obtains in the n512noRT simulation, modulating the filtering scale and suppressing small-scale power.

The suppression of small-scale power in our radiation transfer model may be degenerate with other effects such as the free streaming of warm dark matter particles (Viel et al. 2013a). Our simulations therefore suggest that accounting for inhomogeneous reionization will *tighten* constraints on such processes (for example, by increasing the minimum permitted warm dark matter particle mass). The slight preference in the smallest-scale bin that is observed for the homogeneous reionization history, if confirmed, could point to the need for a more sudden reionization history or else significantly more uniform pre-reionization heating, perhaps owing to X-ray heating (which we do not currently account for).

The comparison in Figure 12 suffers from limitations associated with our finite simulation volume ($12h^{-1}\text{Mpc}$) and limited mass resolution, both of which are known to grow increasingly important at high redshift (Bolton & Becker 2009). Fortunately, published studies suggest that resolution and volume limitations are likely at the $\sim 5\%$ level in our case (Viel et al. 2013a; Oñorbe et al. 2017). Perhaps more worryingly, our simulated mean transmission at $z = 5.4$ requires a significant correction in order to match the observed τ_{eff} ; this correction cannot remove changes to the filtering scale (Lukić et al. 2015). If the simulated end-game to reionization is indeed too slow, then accelerating it (by boosting the ionizing emissivity at $z < 6$) would likely suppress large-scale power.

We note additionally that, while it is possible that galactic winds boost large-scale power at $z < 4$ by modulating the distribution of gas densities within the density range that the LAF probes, they are not expected to be important at $z > 5$. This is because the LAF at higher redshifts traces underdense gas, which is located predominantly far from the galaxies (Viel et al. 2013b).

3.7 CGM

Observations of the CGM complement the IGM at $z > 5$, where the LAF traces predominantly underdense gas. The CGM is moreover a strong observational probe of UVB fluctuations (Oppenheimer et al. 2009; Finlator et al. 2015). On spatial scales larger than a galaxy, the UVB amplitude at the Lyman limit is believed to be relatively homogeneous below $z < 5$, but it was inhomogeneous at earlier times (Worseck et al. 2014; Becker et al. 2015b, 2018; Bosman et al. 2018). Spatial fluctuations on scales larger than a galaxy may boost the fraction of CGM metals that are in high ionization states such as CIV and SiIV. On scales that are smaller than Lyman-limit systems ($\sim 10\text{kpc}$; Schaye 2001), the UVB is suppressed by self-shielding in overdense systems. Our simulations account for both effects in a frequency-dependent way. We have previously shown that local UVB enhancements boost the CIV abundance while self-shielding boosts the abundance of low-ionization ions such as OI, CII, and SiII (Finlator et al. 2013, 2015). Here, we revisit these observational comparisons in the light of our newer model, which contains numerous physical improvements, reproduces observations of the galaxy abundance more faithfully, and sports an enhanced dynamic range.

We generate mock spectra by passing a sightline through our simulation volume that is oblique to its boundaries and wraps around them until it subtends an absorption path length of roughly 420. The temperature, den-

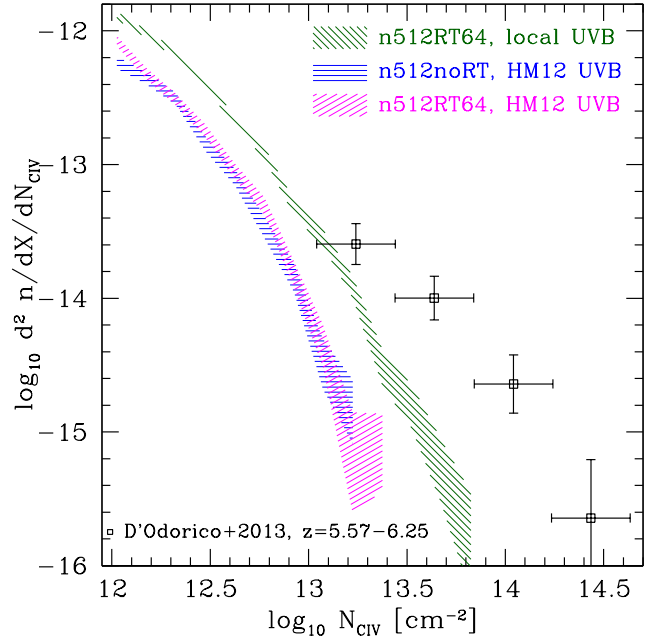


Figure 14. Simulated CIV column density distribution at $z = 5.75$ as compared to observations. The more intense UVB at > 4 Ryd predicted by *Technicolor Dawn* boosts the predicted CIV abundance by ≈ 0.3 dex, alleviating but not removing tension with observations. The simulated distributions are not adjusted to account for observational completeness, which is $> 60\%$ for $\log(N_{\text{CIV}}) > 13.3$ (D’Odorico et al. 2013).

sity, metallicity, and proper velocities of gas particles are smoothed onto the sightline into pixels with a proper velocity width of 2 km s^{-1} . The temperature of multi-phase star-forming gas particles is set to 5000 K ⁷. The ionization state for each metal species is computed using an ionization equilibrium calculation that takes all relevant reactions into account (see Finlator et al. 2015 for details). The UVB is either the local UVB computed directly by the simulation including our self-shielding treatment, or else the spatially-homogeneous Haardt & Madau (2012) UVB. We then compute the simulated optical depth along the sightline following Theuns et al. (1998). Finally, we smooth the spectrum with a gaussian response function with a full-width at half-maximum of 10 km s^{-1} and add gaussian noise corresponding to a signal-to-noise of 50 per pixel. The simulated spectra therefore have an effective resolution of $R = 30,000$.

We extract catalogs of simulated metal absorbers by searching for regions where the flux over at least three consecutive pixels drops 5σ below the continuum. The total column density for each simulated absorber is then computed following Savage & Sembach (1991). We merge the column densities and equivalent widths of individual absorbers whose flux-weighted mean velocities are closer than 50 km s^{-1} into absorption systems to produce model catalogs (e.g., Songaila 2001).

We begin in Figure 14 by examining the CIV column

⁷ Varying this temperature within the range $1000\text{--}20,000 \text{ K}$ has negligible impact on the predicted CII and CIV column density distributions because these species do not trace star-forming gas.

density distribution (CDD) from a conventional simulation (n512noRT) in which the HM12 UVB is assumed both during the simulation and in post-processing (blue horizontal hatches). This underpredicts the observed CIV at all column densities, suggesting either that too few metals are ejected or that the UVB is too weak or too soft. Next, we consider our radiation hydrodynamic simulation with a realistic, spatially-inhomogeneous UVB (n512RT64; green downward hatches). This simulation generates fewer stars (and hence fewer metals) after $z < 15$ (Figure 2) and its UVB amplitude at the Lyman limit is slightly lower than the HM12 UVB at $z = 5.75$ (Table 1). Nevertheless, it yields 0.3–0.4 dex *more* CIV at all columns, bringing the prediction at the highest columns within a factor of \approx six of observations. In order to verify that it is the UVB that dominates this difference, we re-extract metal absorbers from the n512RT64 simulation after substituting the HM12 UVB in place of the simulated one (magenta upward hatches). This yields essentially the same absorber population as the n512noRT model, confirming that enhanced flux at > 4 Ryd dominates the CIV enhancement in our n512RT64 simulation.

Recently, several works have pointed out that conventional hydrodynamic simulations have difficulty reproducing the observed CIV abundance at high redshift (Keating et al. 2016; Bird et al. 2016; Rahmati et al. 2016). Our results are qualitatively similar but with important differences. Whereas complementary efforts such as the Sherwood and Illustris simulations reproduce the observed SMF (for example, Figure 1 of Keating et al. 2016) but adopt the weak He II-ionizing background in the HM12 model, our simulations produce somewhat fewer stars but predict a harder UVB (figure 9). This raises the question as to whether simulations predict a diffuse CGM that is underenriched, underionized, or both.

It is not likely that the gap can be eliminated through further boosts to the outflow velocities because the assumed outflows already contain roughly six times as much kinetic energy as occurs naturally in zoom simulations (Muratov et al. 2015). On the other hand, *weakening* outflows in order to improve agreement with the SMF at $z > 5$ would boost the CGM metallicity (Rahmati et al. 2016). Even this may not be enough though: Figure 4 suggests that the stellar mass density and hence the overall metallicity may be low by as \approx a factor of two, but a factor of two increase in the abundance of strong CIV systems would not bring the prediction within the 1σ confidence interval. Nor can we improve agreement through simple adjustments to the metal yield: boosting the carbon yield would exacerbate tension with the observed abundance of weak C II absorbers (although it would help with the strong ones; Figure 16) as well as with observations of DLA metallicities (Figure 6). In short, if underenrichment is the problem, it is not easy to see how it can be resolved through adjustments to our subgrid models for feedback and enrichment.

The alternative explanation is that our model underproduces CIV because the CGM’s carbon remains underionized, even when we account for a stronger background at > 4 Ryd from quasars (Figure 9) as well as small-scale UVB fluctuations. If the predicted CGM is underionized, this cannot owe to resolution limitations as our simulations resolve the relevant UVB fluctuations spatially: the mean free path at $z = 6$ for photons with energies greater than 4 Ryd in gas that it

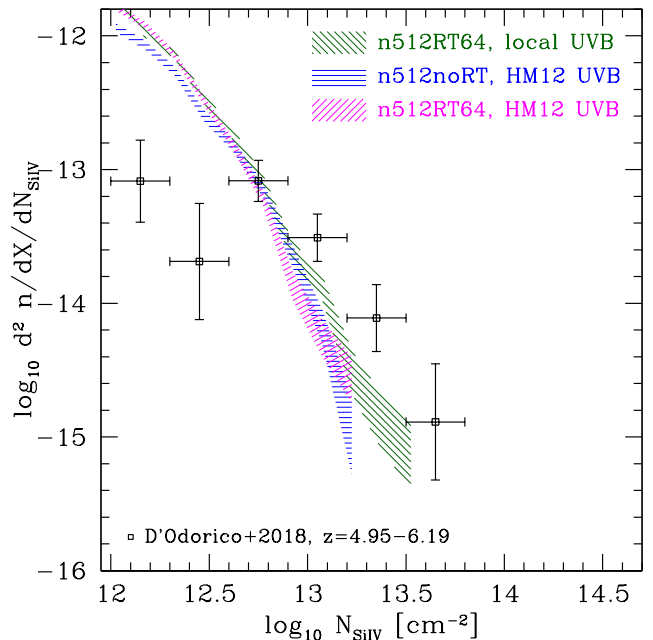


Figure 15. The simulated Si IV column density distribution is in reasonable agreement with observations at $z = 5.75$ irrespective of the choice of UVB. The flattening in the observed distribution at $\log(N_{\text{SiIV}}) < 12.9$ likely reflects observational incompleteness, which is not modeled (see text).

is at least 99% ionized exceeds 1Mpc (proper), while the RT voxels in our n512RT64 simulation are ≈ 40 kpc wide. On the other hand, it is possible that the true UVB is brighter in He II-ionizing energies than we predict owing to a stronger contribution from low-metallicity stars; we will return to this point in Section 4.2.

Finally, we note a possible contribution from the fact that our post-processing calculations assume ionization equilibrium. Relaxing this assumption would change the CIV abundance, although it is difficult to predict in what direction (Oppenheimer & Schaye 2013).

Si IV is a useful complement to CIV because its first ionization potential is only 3.3 Ryd as compared to 4.7 Ryd for CIV (Figure 9). Consequently, its evolution is only weakly sensitive to the progress of He II reionization and to the contribution of quasars. In Figure 15, we show the Si IV CDD at $z = 5.75$ using the simulated and HM12 UVBs as in Figure 14. Observations are from D’Odorico et al. 2018 (in preparation).

The observed CDD shows nonmonotonic behavior for $\log_{10}(N_{\text{SiIV}}) < 12.7$, which we attribute to observational completeness. Although rigorous evaluation of completeness is in-progress, we estimate it by assuming that the data probe to a similar optical depth as the CIV measurements presented in D’Odorico et al. (2013), which are in turn 60% complete for $\log_{10}(N_{\text{CIV}}) = 13.3$. By computing the Si IV column density for which the $\lambda 1393\text{\AA}$ line yields the same optical depth as the 1548\AA line from an absorber with $\log_{10}(N_{\text{CIV}}) = 13.3$, we estimate that the Si IV data are 60% complete at $\log_{10}(N_{\text{SiIV}}) = 12.9$, roughly the column density below which the observed CDD flattens.

Encouragingly, the predicted Si IV CDD agrees with ob-

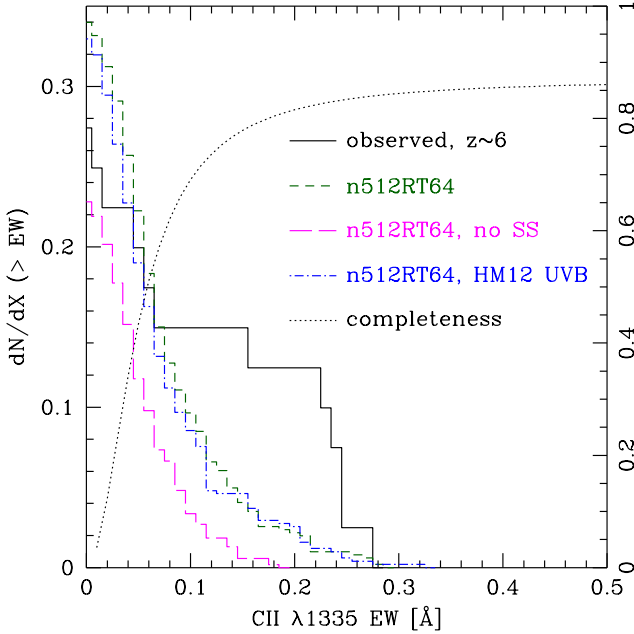


Figure 16. The simulated CII equivalent width distribution at $z = 5.75$ as compared to observations (Becker et al. 2011b; Bosman et al. 2017). Agreement is reasonable at low equivalent widths, but the model underproduces strong CII absorbers.

servations at the 2σ level wherever the observations are reasonably complete and irrespective of the choice of UVB. The insensitivity to the choice of UVB confirms that the progress of He II reionization does not impact Si IV, which is instead a joint tracer of metal production and the growth of the UVB at HI-ionizing energies. Although we do not demonstrate this, adjusting our feedback scheme to boost the overall star formation rate efficiency by $\sim 50\%$, which is observationally permitted (Figures 3–4), would eliminate the outstanding discrepancy with observations.

A thorough assessment of our simulated CGM requires us to consider both high- and low-ionization absorbers such as CII, SiII, and OI because they trace different gas phases and different portions of the UVB. For example, CII complements CIV in that it is sensitive primarily to photons with energies of < 4 Ryd (Figure 9). Moreover, it is sensitive to the progress of hydrogen reionization via charge-exchange reactions with neutral hydrogen. An array of theoretical studies have found that, while the abundance of high-redshift CIV absorbers is difficult to reproduce in cosmological simulations, the predicted abundance of low-ionization absorbers is relatively insensitive to the details of star formation feedback and generally in better agreement with observations than the CIV CDD (for example, Keating et al. 2016).

We evaluate in Figure 16 how our simulated CII equivalent width distributions compare to observations. In order to generate the observed distribution (solid black), we correct the reported survey’s absorption path length by Becker et al. (2011b) of 39.5 to our cosmology, yielding 37.2. We also fold in the results from Bosman et al. (2017), who found one CII absorber with a rest-frame equivalent width of 0.0368 \AA along the line of sight to a quasar at $z = 7.084$ that surveyed an absorption path length of

$\Delta X = 2.906$. We correct the *simulated* absorber abundances (at $z = 5.75$) down in a way that mimics observational incompleteness following Keating et al. (2016): we first fit a function of the form

$$f(x) = \frac{L}{1 + \exp(-k(x - x_0))} \quad (14)$$

to the results displayed in Figure 11 of Becker et al. (2011b) and take x as $\log_{10}(\text{EW}_{\text{OI}})$. Our fit parameters are $(L, k, x_0) = (87\%, 4.5, -1.3)$. We then weight each simulated absorber by the observational completeness at its equivalent width based on Equation 14. This fit is given by the dotted line and the right y-axis in Figures 16–17.

Our simulations (green short-dashed) reproduce the observed abundance of absorbers to within a factor of 3 at all equivalent widths where measurements are available. Given that the factors that govern these predictions such as metal yields, galactic outflow rates, initial mass function, and quasar emissivities were not tuned to match these observations, this level of agreement is remarkable. In detail, our simulations overproduce the abundance of absorbers that are weaker than the estimated 50% completeness limit and underproduce the stronger systems.

We evaluate the impact of local UVB fluctuations on CII as in the case of CIV, by replacing the simulated UVB with the HM12 UVB (blue dot-dashed) in post-processing. Surprisingly, the resulting predicted distribution is largely unchanged. While this agreement is nominally expected given the close correspondence between the HM12 and the volume-averaged simulated UVB near the Lyman limit (Figure 8), it hides a near-complete cancellation between short-range UVB amplifications and self-shielding. If we neglect self-shielding in post-processing (magenta long-dashed), then there is significantly less CII at all equivalent widths. This, in turn, implies that modeling CII in a way that accounts for self-shielding of dense gas but *neglects* UVB amplifications may artificially inflate the predicted CII abundance.

Neutral oxygen traces a denser gas phase than the other ions, hence its abundance is a more direct probe of the gradual encroachment of the UVB into the CGM (Keating et al. 2014). In Figure 17, we compare our simulation versus the observed cumulative distribution of OI equivalent widths at $z \sim 6$ (Becker et al. 2011b; Bosman et al. 2017). In order to generate the observed distribution (solid black), we treat the upper limit on the OI equivalent width of the system along the line of sight to J1630+4012 as a detection. We also add $\Delta X = 2.00926$ to the absorption path length in order to account for the fact that Bosman et al. (2017) uncovered no OI absorbers along the path to a quasar at $z = 7.084$.

The result of this comparison is quite similar to Figure 16: our simulation overproduces weak absorbers, produces roughly the correct number at the 50% observational completeness limit, and underproduces the strong ones.⁸

We now consider why the predicted shape of our low-ionization absorber equivalent width distributions may be too steep. The comparison in Figure 17 does not obviously

⁸ Note that it is not useful to vary the UVB in post-processing with OI as we did with CII because it is charge-locked to HI, whose nonequilibrium ionization state is adopted directly from the simulation.

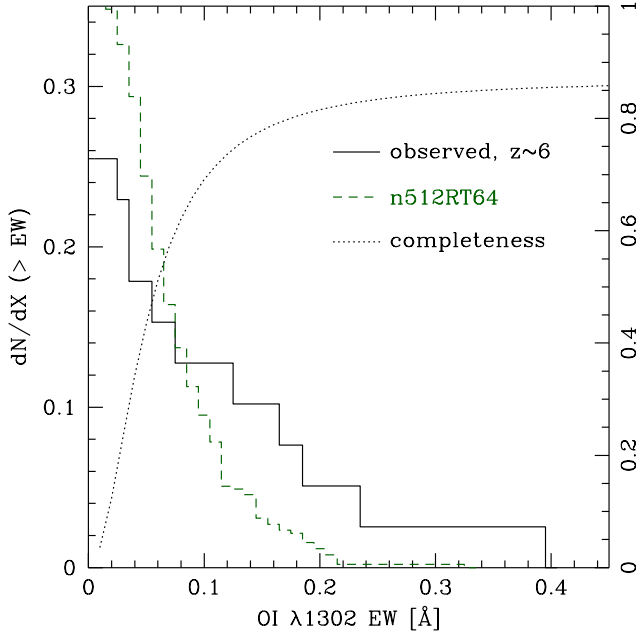


Figure 17. The simulated OI equivalent width distribution at $z = 5.75$ is in tolerable agreement with observations of weak absorbers $z \sim 6$ (Becker et al. 2011b; Bosman et al. 2017) but may underproduce strong systems. The observed and simulated curves were generated in a similar way to Figure 16.

imply that the simulated oxygen yields are low: boosting the metal yield would, to first order, shift the entire curve to higher equivalent widths without changing its shape. Agreement at strong equivalent widths would come at the cost of overproducing the abundance of well-sampled weak systems. Moreover, our metal yields are, in a sense, already boosted by our assumption that 50% of SNe explode as hypernovae (Nomoto et al. 2006), and further boosts would, as before, exacerbate tension with observations of DLA metallicities.

Another possible explanation for the overabundance of weak low-ionization systems may be inaccuracy in our adopted model for galactic outflows. To address this, we refer to Keating et al. (2016), who explored how a number of models for hydrodynamic feedback, UVB amplitude, and self-shielding impact the predicted absorber abundances. They found that weak CII absorbers ($EW < 0.1 \text{ \AA}$) are strongly overproduced in their *HVEL* model, which imposes a minimum outflow velocity of 600 km s^{-1} . This suggests that our simulated outflows may be too fast (Equation 3). Suppressing the outflow velocities may reduce the predicted CII abundance into better agreement with observations—but at the cost of cutting the numbers of CIV and SiIV absorbers, which are already low. The impact of changing outflow velocities on the predicted OI abundance will be generally weaker (Keating et al. 2016), although it will likely improve agreement. Likewise, it would improve agreement with the observed UV LF (Figure 3).

Alternatively, the overabundance of weak low-ionization absorbers may owe to the UVB, which disproportionately affects weak systems. Strengthening it would preferentially

suppress weak CII and OI systems while boosting weak CIV systems (Keating et al. 2016, Figure 10).

Finally, it is always possible that the observationally-inferred completeness is too high owing to an inaccurate model for weak absorbers. To this end, it would be interesting to explore how the predicted profiles of weak absorbers compare with conventional assumptions; however, we defer this to future work.

In summary, Figures 14–17 show that our simulations roughly reproduce the observed abundance of weak CIV, SiIV, CII, and OI absorbers at $z \sim 6$ while underproducing the strong systems in the same ions. We are thus confronted with the odd result that, while CIV seems to require that the CGM near galaxies be more highly-ionized, CII and OI require it to be more neutral! The overall good agreement among the weak systems corroborates the relatively good agreement in Figure 6 in suggesting that the CGM’s metal enrichment is realistic. In detail, however, the tendency for the simulated equivalent width distributions to be too steep irrespective of the ion suggests non-trivial issues with wind speed, UVB, and overall CGM metallicity.

4 SUMMARY AND DISCUSSION

4.1 Summary

The *Technicolor Dawn* simulations combine a model for star- and galaxy- formation that is anchored in high-resolution simulations with an on-the-fly multifrequency radiation transport solver so that galaxies, their CGM, the IGM, the UVB, and reionization are all followed simultaneously. Their predictions are subject to only one parameter that has been tuned to match observations in a precise way, $f_{\text{esc,gal}}(z)$, hence they represent a unified statement of how well the reigning galaxy-driven reionization scenario can account for a wide variety of observations of the reionization epoch and its immediate aftermath. We have, of course, explored only a subset of the available observations, but our results so far already raise some interesting questions.

The predicted history of star formation is consistent with observations, which is encouraging given that the agreement does not represent empirical calibration. In detail, comparisons with the observed UV LF and SMF indicate that star formation is oversuppressed by up to a factor of 2 at $z > 5$, with larger discrepancies at higher resolution. The predicted M_* -SFR relationship is reasonably robust to resolution effects (although see Schaye et al. 2015), and is consistent with observations at $z \sim 6$ within the uncertainty, suggesting that the UV LF and SMF discrepancies share a common origin. These results are largely insensitive to the progress of reionization because observed galaxies live in haloes that are too massive for photoionization feedback.

Turning to reionization, the model for $f_{\text{esc,gal}}(z)$ that we adopt falls from 35–50% at early times to $< 20\%$ by $z = 5$. The values at $z > 6$ are higher than observations and some complementary models indicate, but have been observed directly in isolated galaxies. Adopting this model yields a reionization history that is in broad agreement with observations of the volume-averaged neutral hydrogen fraction and the hydrogen ionization rate at the close of the hydrogen reionization epoch. Curiously, our low-resolution n256RT32

simulation yields marginally better agreement with observations of $X_{\text{H I, V}}(z)$ while underproducing Γ_{HI} , whilst our high-resolution n512RT64 simulation is in excellent agreement with Γ_{HI} and marginally underproduces $X_{\text{H I, V}}(z)$. The mean transmission in the n512RT64 simulation is systematically low for $z < 5.7$, though not as low as in the case of the HM12 UVB. This problem, which appears generic to hydrodynamic simulations of reionization, could indicate the need for very large-scale UVB fluctuations (Becker et al. 2018), a hotter IGM, or systematic uncertainties in the observations.

The UVB that drives reionization is spectrally-soft, corresponding to less than 5 eV of IGM heating per photoionization. Owing to this tepid heating, the observed Lyman- α flux power spectrum is reproduced at all but the largest k -bin, where it may be 1.5σ high. In detail, however, a tendency for inhomogeneous reionization to boost large-scale power and suppress small-scale power suggests that current measurements contain untapped clues into large-scale UVB fluctuations, small-scale scatter in the ρ - T distribution, and possibly even the early stages of He II reionization; simulations such as the *Technicolor Dawn* suite will be crucial in unlocking these secrets.

The simulated ρ - T relationship at $z = 5.4$ shows significantly enhanced scatter with respect to a uniform-UVB model, as expected in the immediate aftermath of reionization. This scatter suppresses small-scale LAF fluctuations, although the largest differences with respect to a uniform-UVB model are at scales that have not yet been measured directly.

Finally, simulated galactic outflows disperse enough metals into the CGM to yield DLA metallicities that are consistent with observations at $z \sim 5$, although there may be evidence that simulated DLAs are systematically overenriched at the factor-of-two level. There is an underabundance of strong CIV, CII, and OI absorbers and a possible excess of weak CII and OI absorbers. The predicted CIV abundance is significantly enhanced by the harder *Technicolor Dawn* UVB, though not enough to match observations. CII is unaffected by UVB fluctuations owing to a near-perfect cancellation between the effects of living near ionizing sources (i.e., galaxies) and originating in self-shielded gas. The SiIV CDD is $\approx 1\sigma$ low at the highest observed columns and in agreement at lower columns, significantly better than CIV.

4.2 Discussion

The results that the *Technicolor Dawn* simulations underproduce stars and strong OI, CII, and SiIV absorbers could all point to the same problem, namely that our subgrid prescription for generating galactic outflows (Equations 2 and 3) is too vigorous. Moderating either the mass-loading factor or the wind launch velocity would both boost star formation and enhance the abundance of strong metal absorbers (Rahmati et al. 2016).

Such tuning would not be inconsistent with results from high-resolution simulations: Muratov et al. (2015) assign to the normalization of Equation 2 an uncertainty of 0.2 dex. Reducing it by this factor would significantly alleviate discrepancies. Reducing the wind launch velocities would additionally reduce the predicted abundance of weak low-ionization absorbers (Keating et al. 2016), improving agree-

ment with observations. At the same time, the extra star formation would allow us to lower $f_{\text{esc,gal}}(z)$ by a similar factor, bringing it closer to the 5–15% range that seems favored overall by complementary works.

More broadly, however, if the underproduction of stars and strong metal absorbers can be ameliorated by moderating galactic outflows, then they highlight the problems that arise from tying outflow scalings in cosmological simulations too closely to results from high-resolution simulations. In the latter, most of the material that is ejected from galaxies returns on a short timescale while only a fraction escapes to the virial radius (Muratov et al. 2015; Christensen et al. 2016). This broad range of outcomes for ejected gas is not treated realistically by our simulations, which assume a relatively narrow range of launch velocities and use hydrodynamic de-coupling to guarantee that most outflowing gas escapes to the virial radius. These simplifications may contribute to the oversuppression of star formation and metal generation, and calibrating them more carefully would improve agreement with observations.

However, this tuning, by itself, will not bring the predicted abundance of strong CIV absorbers into agreement with observations: With the HM12 UVB, the predicted abundance for $N_{\text{CIV}} > 10^{13.5} \text{cm}^{-2}$ is low by a factor of ≈ 10 . Adopting the harder *Technicolor Dawn* UVB, strong CIV absorbers remain low by a factor of 3–6. Closing the remaining gap through further enhancements to metal production would inevitably overproduce strong CII, OI, and SiIV as well as DLA metallicities. Hence while enhancing star formation to the point that the SMF is clearly reproduced will alleviate the discrepancy, it may well leave the need for additional mechanisms for boosting the CIV fraction.

One possibility is that conventional stellar population synthesis models simply underpredict the He II-ionizing continuum from massive, low-metallicity stars. Senchyna et al. (2017) have shown that low-redshift galaxies with metallicities below $Z/Z_{\odot} = 0.2$ produce significantly stronger He II recombination lines than can be explained by the expected ionizing flux from stellar population synthesis models. Likewise, high-resolution observations of high-redshift galaxies indicate rest-frame ultraviolet emission lines including CIV1548, 1550 and HeII1640 that have unaccountably high equivalent widths (for example, Smit et al. 2017; Berg et al. 2018). Given that our most metal-enriched galaxy at $z = 6$ has $Z_*/Z_{\odot} = 0.1$, all of our simulated reionization-epoch galaxies may be too faint at He II-ionizing energies. Accounting for effects associated with binary star evolution would harden the predicted UVB (Stanway et al. 2016). Additionally, it would increase the overall ionizing emissivity (Rosdahl et al. 2018), enabling reionization constraints to be matched with a reduced $f_{\text{esc,gal}}(z)$.

It is worth noting that boosting the emissivity from galaxies at > 4 Ryd will accelerate the early stages of He II reionization. This “second stage” to reionization is conventionally considered to have begun after $z = 5$ (McQuinn et al. 2009; Haardt & Madau 2012). However, in the *Technicolor Dawn* simulations, the He III fraction is predicted to reach 30% by $z = 5$ (see also Ciardi et al. 2012). This is qualitatively consistent with observational suggestions that He II reionization begins too early to be purely quasar-driven (Becker et al. 2011a; Worseck et al. 2016), and it underscores the need for further investigation

into the possible role of galaxies in jump-starting He II reionization.

A final possible method for boosting the CGM’s ionization state involves appealing to the inherently stochastic nature of star formation in dwarf galaxies. Currently, *Technicolor Dawn* bases the emissivity on the gas particles’ instantaneous star formation rates by assuming that they have been forming stars constantly at the current rate for 100 Myr (Section 2). While this can effectively increase the radiation transport solver’s spatial resolution (Rahmati et al. 2013), it misses the dramatic temporal fluctuations that occur when the emissivity is tied to the star particles (Ma et al. 2015). These fluctuations could enhance the CGM’s CIV fraction, particularly if the assumption of ionization equilibrium were relaxed (Oppenheimer & Schaye 2013).

The tendency for the *Technicolor Dawn* simulations to underproduce the mean transmission in the LAF suggests that some measurements of the UVB amplitude may be biased low. At $z = 5.4$, observations indicate that the IGM’s HI photoionization rate $\Gamma_{\text{HI}-13} = 4.7$ (D’Aloisio et al. 2018), 1.3 (Calverley et al. 2011), 1.8–4.7 (Wyithe & Bolton 2011), or 8.5 (Davies et al. 2018b), where $\Gamma_{\text{HI}-13}$ is in units of 10^{-13}s^{-1} . The n512RT64 simulation predicts an ionization rate of 3.2 at the same redshift, within the lower end of the observed range, while underproducing the mean transmission (see also Figure 8). By contrast, the $40h^{-1}\text{Mpc}$ radiation transport simulation of Keating et al. (2018) predicts $\Gamma_{\text{HI}-13} = 6.67$ and overproduces the mean transmission (Table 4 of Bosman et al. 2018). This indicates that, at least qualitatively, a stronger UVB at $z = 5-6$ may solve the problem. At the same time, a stronger UVB would alleviate tension between the simulated and observed CIV CDDs and reduce the predicted DLA abundance, which currently lies at the top of the observed 68% confidence interval (Section 3.2). These considerations all raise the question of whether a stronger Γ_{HI} is observationally permitted, as recently suggested by Davies et al. (2018b).

Systematic uncertainties could readily compromise the comparison between the predicted and inferred UVB amplitude because we quote the actual simulated UVB amplitude rather than the one that would be inferred from our simulated observables. The measured UVB amplitude is model-dependent at the \approx factor-of-two level owing, for example, to uncertainties in the assumed IGM temperature (Section 3.6) or role of ionizing photons released during recombinations, and we have not attempted to correct for these issues. It would be interesting to evaluate this possibility by applying techniques for measuring the IGM temperature and UVB amplitude using realistic, inhomogeneous reionization models. For the present, however, we regard the discrepancy in the mean transmission as the more robust indicator of a problem.

We may condense this discussion into the following questions:

(i) Can the underabundance of strong OI, CII, and SiIV absorbers and the oversuppression of star formation both be resolved by moderating galactic outflows, or do these discrepancies indicate small-scale spatial fluctuations in the CGM temperature and UVB that are not yet numerically resolved?

(ii) If galactic outflows are weakened, does the $f_{\text{esc,gal}}(z)$

that is required for matching the history of reionization fall within agreement with observations and high-resolution simulations?

(iii) Can reionization models simultaneously reproduce the observed mean transmission in the LAF without overproducing the observed HI photoionization rate?

(iv) Do observations that young, low-metallicity galaxies are unaccountably bright in He II emission while their CGM are unaccountably weak in CIV absorption represent the same problem? Can both problems be resolved through enhanced He II-ionizing emission from young galaxies without overheating the IGM? If so, what are the implications for the post-reionization HI LAF and the history of He II reionization, which is conventionally assumed to be entirely quasar-driven (Furlanetto & Oh 2008; Haardt & Madau 2012)?

These considerations emphasize that the conventional, galaxy-driven HI reionization hypothesis contains many unsolved problems. They also illustrate how coupling multi-frequency radiation transport solvers to realistic models for galaxy evolution will allow the synthesis of observations that are normally considered in isolation, likely unveiling qualitatively new synergies and tensions.

ACKNOWLEDGEMENTS

Our simulations were run on NMSU’s JOKER and XSEDE’s COMET supercomputers; for advice and support we thank the NMSU ICT department and XSEDE. We thank Moire Prescott, Caitlin Doughty, Valentina D’Odorico, Zheng Cai, Lise Christensen, and Marc Rafelski for helpful comments and conversations. George Becker we thank particularly warmly for encouragement and helpful comments on the draft. KF thanks Claudia Scarlata for organizing the conference “Distant Galaxies from the Far South”, where the thinking for this work matured significantly. We also thank the anonymous referee for a sharp-eyed and supportive report that improved the paper. Our work made use of the WebPlotDigitizer tool (<https://automeris.io/WebPlotDigitizer>), for which we thank A. Rohatgi. This research would also have been quite impossible without the NASA Astrophysics Data System and the arXiv eprint service. EZ acknowledges funding from the Swedish National Space Board, and LK acknowledges support from a fellowship from the Canadian Institute for Theoretical Astrophysics. The Cosmic Dawn Center is funded by the Danish National Research Foundation.

Z	C	O	Si	Fe	N	Ne	Mg	S	Ca	Ti
0	0.00191541	0.0213646	0.00179892	0.000844243	5.49083e-06	0.00457574	0.00153244	0.000708791	8.15213e-05	1.49848e-06
0.001	0.00111629	0.0222635	0.0016386	0.000891533	9.13731e-05	0.00431286	0.00199825	0.000627048	7.49162e-05	1.60633e-06
0.004	0.00119844	0.0153524	0.00150934	0.000693353	0.000220067	0.00343836	0.00121643	0.000591956	6.75242e-05	1.21226e-06
0.02	0.00193115	0.0148044	0.00121749	0.000768802	0.000680037	0.004222	0.00124573	0.000549918	6.05825e-05	1.60292e-06

Table 2. Our assumed metal yields, computed from [Nomoto et al. \(2006\)](#) assuming a [Kroupa \(2001\)](#) IMF from 0.1–100 M_{\odot} and a 50% hypernova fraction.

f_{HNe}	C	O	Si	Fe	N	Ne	Mg	S	Ca	Ti
0	0.00108745	0.0186467	0.00161469	0.000703623	7.41348e-05	0.00362083	0.0015565	0.00066296	8.10135e-05	1.21059e-06
0.5	0.00111629	0.0222635	0.0016386	0.000891533	9.13731e-05	0.00431286	0.00199825	0.000627048	7.49162e-05	1.60633e-06
1.0	0.00114513	0.0258802	0.00166252	0.00107944	0.000108611	0.00500489	0.00244	0.000591136	6.88188e-05	2.00206e-06

Table 3. The dependence of the metal yield on HNe fraction f_{HNe} for the same IMF as in [Table 3](#) and a stellar population with $Z = 0.001$. The second row is reproduced from [Table 2](#)

REFERENCES

- Ahn K., Iliev I. T., Shapiro P. R., Mellema G., Koda J., Mao Y., 2012, *ApJ*, **756**, L16
- Alvarez M. A., Finlator K., Trenti M., 2012, *ApJ*, **759**, L38
- Angel P. W., Poole G. B., Ludlow A. D., Duffy A. R., Geil P. M., Mutch S. J., Mesinger A., Wyithe J. S. B., 2016, *MNRAS*, **459**, 2106
- Asplund M., Grevesse N., Sauval A. J., Scott P., 2009, *ARA&A*, **47**, 481
- Bañados E., et al., 2018, *Nature*, **553**, 473
- Bahcall J. N., Peebles P. J. E., 1969, *ApJ*, **156**, L7
- Barkana R., Loeb A., 2000, *ApJ*, **539**, 20
- Barkana R., Loeb A., 2004, *ApJ*, **609**, 474
- Becker G. D., Bolton J. S., Haehnelt M. G., Sargent W. L. W., 2011a, *MNRAS*, **410**, 1096
- Becker G. D., Sargent W. L. W., Rauch M., Calverley A. P., 2011b, *ApJ*, **735**, 93
- Becker G. D., Bolton J. S., Lidz A., 2015a, *Publ. Astron. Soc. Australia*, **32**, e045
- Becker G. D., Bolton J. S., Madau P., Pettini M., Ryan-Weber E. V., Venemans B. P., 2015b, *MNRAS*, **447**, 3402
- Becker G. D., Davies F. B., Furlanetto S. R., Malkan M. A., Boera E., Douglass C., 2018, preprint, ([arXiv:1803.08932](https://arxiv.org/abs/1803.08932))
- Berg D. A., Erb D. K., Auger M. W., Pettini M., Brammer G. B., 2018, preprint, ([arXiv:1803.02340](https://arxiv.org/abs/1803.02340))
- Bird S., Rubin K. H. R., Suresh J., Hernquist L., 2016, *MNRAS*, **462**, 307
- Bird S., Garnett R., Ho S., 2017, *MNRAS*, **466**, 2111
- Bolton J. S., Becker G. D., 2009, *MNRAS*, **398**, L26
- Bolton J. S., Haehnelt M. G., 2007, *MNRAS*, **382**, 325
- Bosman S. E. I., Becker G. D., Haehnelt M. G., Hewett P. C., McMahon R. G., Mortlock D. J., Simpson C., Venemans B. P., 2017, *MNRAS*, **470**, 1919
- Bosman S. E. I., Fan X., Jiang L., Reed S. L., Matsuoka Y., Becker G. D., Haehnelt M. G., 2018, preprint, ([arXiv:1802.08177](https://arxiv.org/abs/1802.08177))
- Bouwens R. J., et al., 2015, *ApJ*, **803**, 34
- Bryan G. L., Norman M. L., 1998, *ApJ*, **495**, 80
- Cai Z., Fan X., Dave R., Finlator K., Oppenheimer B., 2017, *ApJ*, **849**, L18
- Calverley A. P., Becker G. D., Haehnelt M. G., Bolton J. S., 2011, *MNRAS*, **412**, 2543
- Chabrier G., 2003, *PASP*, **115**, 763
- Chardin J., Haehnelt M. G., Aubert D., Puchwein E., 2015, *MNRAS*, **453**, 2943
- Chen P., Norman M. L., Xu H., Wise J. H., 2017a, preprint, ([arXiv:1705.00026](https://arxiv.org/abs/1705.00026))
- Chen S.-F. S., et al., 2017b, *ApJ*, **850**, 188
- Chisholm J., Tremonti C. A., Leitherer C., Chen Y., Wofford A., Lundgren B., 2015, *ApJ*, **811**, 149
- Christensen C. R., Davé R., Governato F., Pontzen A., Brooks A., Munshi F., Quinn T., Wadsley J., 2016, *ApJ*, **824**, 57
- Ciardì B., Bolton J. S., Maselli A., Graziani L., 2012, *MNRAS*, **423**, 558
- Conroy C., Gunn J. E., White M., 2009, *ApJ*, **699**, 486
- Cooke R., Pettini M., Steidel C. C., Rudie G. C., Nissen P. E., 2011, *MNRAS*, **417**, 1534
- Cristiani S., Serrano L. M., Fontanot F., Vanzella E., Monaco P., 2016, *MNRAS*, **462**, 2478
- Crowther P. A., et al., 2016, *MNRAS*, **458**, 624
- D'Aloisio A., McQuinn M., Trac H., 2015, *ApJ*, **813**, L38
- D'Aloisio A., Upton Sanderbeck P. R., McQuinn M., Trac H., Shapiro P. R., 2017, *MNRAS*, **468**, 4691
- D'Aloisio A., McQuinn M., Davies F. B., Furlanetto S. R., 2018, *MNRAS*, **473**, 560
- D'Odorico V., et al., 2013, *MNRAS*, **435**, 1198
- Davé R., Thompson R., Hopkins P. F., 2016, *MNRAS*, **462**, 3265
- Davies F. B., Becker G. D., Furlanetto S. R., 2017, preprint, ([arXiv:1708.08927](https://arxiv.org/abs/1708.08927))
- Davies F. B., et al., 2018a, preprint, ([arXiv:1802.06066](https://arxiv.org/abs/1802.06066))
- Davies F. B., Hennawi J. F., Eilers A.-C., Lukić Z., 2018b, *ApJ*, **855**, 106
- Díaz C. G., Koyama Y., Ryan-Weber E. V., Cooke J., Ouchi M., Shimasaku K., Nakata F., 2014, *MNRAS*, **442**, 946
- Doussot A., Trac H., Cen R., 2017, preprint, ([arXiv:1712.04464](https://arxiv.org/abs/1712.04464))
- Duncan K., et al., 2014, *MNRAS*, **444**, 2960
- Faisst A. L., 2016, *ApJ*, **829**, 99
- Faucher-Giguère C.-A., Lidz A., Zaldarriaga M., Hernquist L., 2009, *ApJ*, **703**, 1416
- Finkelstein S. L., et al., 2015, *ApJ*, **810**, 71
- Finlator K., Özel F., Davé R., 2009, *MNRAS*, **393**, 1090
- Finlator K., Davé R., Özel F., 2011, *ApJ*, **743**, 169
- Finlator K., Muñoz J. A., Oppenheimer B. D., Oh S. P., Özel F., Davé R., 2013, *MNRAS*, **436**, 1818
- Finlator K., Thompson R., Huang S., Davé R., Zackrisson E., Oppenheimer B. D., 2015, *MNRAS*, **447**, 2526
- Finlator K., Oppenheimer B. D., Davé R., Zackrisson E., Thompson R., Huang S., 2016, *MNRAS*, **459**, 2299
- Finlator K., et al., 2017, *MNRAS*, **464**, 1633
- Fontanot F., Hirschmann M., De Lucia G., 2017, *ApJ*, **842**, L14
- Furlanetto S. R., Oh S. P., 2008, *ApJ*, **681**, 1
- Furlanetto S. R., Oh S. P., 2009, *ApJ*, **701**, 94
- Garzilli A., Boyarsky A., Ruchayskiy O., 2017, *Physics Letters B*, **773**, 258
- Gnedin N. Y., 2014, *ApJ*, **793**, 29
- Gnedin N. Y., Abel T., 2001, *New Astron.*, **6**, 437
- Gnedin N. Y., Hamilton A. J. S., 2002, *MNRAS*, **334**, 107
- Gnedin N. Y., Ostriker J. P., 1997, *ApJ*, **486**, 581
- Gnedin N. Y., Becker G. D., Fan X., 2017, *ApJ*, **841**, 26
- Grazian A., et al., 2015, *A&A*, **575**, A96
- Grazian A., et al., 2018, *A&A*, **613**, A44
- Greif T. H., Bromm V., 2006, *MNRAS*, **373**, 128
- Greig B., Mesinger A., Haiman Z., Simcoe R. A., 2017, *MNRAS*, **466**, 4239
- Haardt F., Madau P., 2012, *ApJ*, **746**, 125
- Haehnelt M. G., Steinmetz M., Rauch M., 1998, *ApJ*, **495**, 647
- Hahn O., Abel T., 2011, *MNRAS*, **415**, 2101
- Hassan S., Davé R., Mitra S., Finlator K., Ciardi B., Santos M. G., 2018, *MNRAS*, **473**, 227
- Heringer E., Pritchett C., Kezwer J., Graham M. L., Sand D., Bildfell C., 2017, *ApJ*, **834**, 15
- Hopkins P. F., 2013, *MNRAS*, **428**, 2840
- Huang K.-H., et al., 2017, *ApJ*, **838**, 6
- Hui L., Gnedin N. Y., 1997, *MNRAS*, **292**, 27
- Iliev I. T., Mellema G., Ahn K., Shapiro P. R., Mao Y., Pen U.-L., 2014, *MNRAS*, **439**, 725
- Inoue A. K., et al., 2018, preprint, ([arXiv:1801.00067](https://arxiv.org/abs/1801.00067))
- Izotov Y. I., Schaerer D., Worseck G., Guseva N. G., Thuan T. X., Verhamme A., Orlitová I., Fricke K. J., 2018, *MNRAS*, **474**, 4514
- Kakiichi K., et al., 2018, preprint, ([arXiv:1803.02981](https://arxiv.org/abs/1803.02981))
- Katz N., Weinberg D. H., Hernquist L., 1996, *ApJS*, **105**, 19
- Katz H., Kimm T., Haehnelt M., Sijacki D., Rosdahl J., Blaizot J., 2018, *MNRAS*, **478**, 4986
- Keating L. C., Haehnelt M. G., Becker G. D., Bolton J. S., 2014, *MNRAS*, **438**, 1820
- Keating L. C., Puchwein E., Haehnelt M. G., Bird S., Bolton J. S., 2016, *MNRAS*, **461**, 606
- Keating L. C., Puchwein E., Haehnelt M. G., 2018, *MNRAS*, **477**, 5501
- Khaire V., Srianand R., Choudhury T. R., Gaikwad P., 2016, *MNRAS*, **457**, 4051
- Konno A., et al., 2018, *PASJ*, **70**, S16
- Kroupa P., 2001, *MNRAS*, **322**, 231
- Kuhlen M., Faucher-Giguère C.-A., 2012, *MNRAS*, **423**, 862
- Leitherer C., et al., 1999, *ApJS*, **123**, 3

- Livermore R. C., Finkelstein S. L., Lotz J. M., 2017, *ApJ*, **835**, 113
- Lukić Z., Stark C. W., Nugent P., White M., Meiksin A. A., Almgren A., 2015, *MNRAS*, **446**, 3697
- Lusso E., Worseck G., Hennawi J. F., Prochaska J. X., Vignali C., Stern J., O’Meara J. M., 2015, *MNRAS*, **449**, 4204
- Ma X., Kasen D., Hopkins P. F., Faucher-Giguère C.-A., Quataert E., Kereš D., Murray N., 2015, *MNRAS*, **453**, 960
- Madau P., 2017, *ApJ*, **851**, 50
- Madau P., Dickinson M., 2014, *ARA&A*, **52**, 415
- Madau P., Haardt F., 2015, *ApJ*, **813**, L8
- Maeda K., Röpke F. K., Fink M., Hillebrandt W., Travaglio C., Thielemann F.-K., 2010, *ApJ*, **712**, 624
- Manti S., Gallerani S., Ferrara A., Greig B., Feruglio C., 2017, *MNRAS*, **466**, 1160
- Mason C. A., Treu T., Dijkstra M., Mesinger A., Trenti M., Pentericci L., de Barros S., Vanzella E., 2018, *ApJ*, **856**, 2
- McGreer I. D., Mesinger A., D’Odorico V., 2015, *Monthly Notices of the Royal Astronomical Society*, **447**, 499
- McGreer I. D., Fan X., Jiang L., Cai Z., 2018, *AJ*, **155**, 131
- McQuinn M., 2016, *ARA&A*, **54**, 313
- McQuinn M., Lidz A., Zaldarriaga M., Hernquist L., Hopkins P. F., Dutta S., Faucher-Giguère C.-A., 2009, *ApJ*, **694**, 842
- Micheva G., Iwata I., Inoue A. K., 2017, *MNRAS*, **465**, 302
- Mitra S., Choudhury T. R., Ferrara A., 2015, *MNRAS*, **454**, L76
- Muratov A. L., Kereš D., Faucher-Giguère C.-A., Hopkins P. F., Quataert E., Murray N., 2015, *MNRAS*, **454**, 2691
- Navarro J. F., Frenk C. S., White S. D. M., 1996, *ApJ*, **462**, 563
- Nomoto K., Tominaga N., Umeda H., Kobayashi C., Maeda K., 2006, *Nuclear Physics A*, **777**, 424
- Oñorbe J., Hennawi J. F., Lukić Z., Walther M., 2017, *ApJ*, **847**, 63
- Oh S. P., 2002, *MNRAS*, **336**, 1021
- Okamoto T., Gao L., Theuns T., 2008, *MNRAS*, **390**, 920
- Oppenheimer B. D., Davé R., 2008, *MNRAS*, **387**, 577
- Oppenheimer B. D., Schaye J., 2013, *MNRAS*, **434**, 1063
- Oppenheimer B. D., Davé R., Finlator K., 2009, *MNRAS*, **396**, 729
- Ouchi M., et al., 2018, *PASJ*, **70**, S13
- Paardekooper J.-P., Khochfar S., Dalla Vecchia C., 2015, *MNRAS*, **451**, 2544
- Parsa S., Dunlop J. S., McLure R. J., 2018, *MNRAS*, **474**, 2904
- Pawlik A. H., Schaye J., 2009, *MNRAS*, **396**, L46
- Planck Collaboration et al., 2016a, *A&A*, **594**, A13
- Planck Collaboration et al., 2016b, *A&A*, **596**, A108
- Poudel S., Kulkarni V. P., Morrison S., Péroux C., Som D., Rahmani H., Quiret S., 2018, *MNRAS*, **473**, 3559
- Price L. C., Trac H., Cen R., 2016, preprint, ([arXiv:1605.03970](https://arxiv.org/abs/1605.03970))
- Puchwein E., Bolton J. S., Haehnelt M. G., Madau P., Becker G. D., Haardt F., 2015, *MNRAS*, **450**, 4081
- Qin Y., et al., 2017, *MNRAS*, **472**, 2009
- Rafelski M., Wolfe A. M., Prochaska J. X., Neeleman M., Mendez A. J., 2012, *ApJ*, **755**, 89
- Rafelski M., Neeleman M., Fumagalli M., Wolfe A. M., Prochaska J. X., 2014, *ApJ*, **782**, L29
- Rahmati A., Schaye J., Pawlik A. H., Raičević M., 2013, *MNRAS*, **431**, 2261
- Rahmati A., Schaye J., Crain R. A., Oppenheimer B. D., Schaller M., Theuns T., 2016, *MNRAS*, **459**, 310
- Raiter A., Schaerer D., Fosbury R. A. E., 2010, *A&A*, **523**, A64
- Ricotti M., Ostriker J. P., 2004, *MNRAS*, **350**, 539
- Rosdahl J., et al., 2018, preprint, ([arXiv:1801.07259](https://arxiv.org/abs/1801.07259))
- Rutkowski M. J., et al., 2017, *ApJ*, **841**, L27
- Salmon B., et al., 2015, *ApJ*, **799**, 183
- Santini P., et al., 2017, *ApJ*, **847**, 76
- Savage B. D., Sembach K. R., 1991, *ApJ*, **379**, 245
- Schaerer D., 2002, *A&A*, **382**, 28
- Schaye J., 2001, *ApJ*, **559**, 507
- Schaye J., et al., 2010, *MNRAS*, **402**, 1536
- Schaye J., et al., 2015, *MNRAS*, **446**, 521
- Schneider F. R. N., et al., 2018, *Science*, **359**, 69
- Senchyna P., et al., 2017, *MNRAS*, **472**, 2608
- Sharma M., Theuns T., Frenk C., Bower R., Crain R., Schaller M., Schaye J., 2016, *MNRAS*, **458**, L94
- Smit R., Swinbank A. M., Massey R., Richard J., Smail I., Kneib J.-P., 2017, *MNRAS*, **467**, 3306
- Somerville R. S., Davé R., 2015, *ARA&A*, **53**, 51
- Song M., et al., 2016, *ApJ*, **825**, 5
- Songaila A., 2001, *ApJ*, **561**, L153
- Springel V., 2005, *MNRAS*, **364**, 1105
- Springel V., Hernquist L., 2003, *MNRAS*, **339**, 289
- Stanway E. R., Eldridge J. J., Becker G. D., 2016, *MNRAS*, **456**, 485
- Steidel C. C., Strom A. L., Pettini M., Rudie G. C., Reddy N. A., Trainor R. F., 2016, *ApJ*, **826**, 159
- Sutherland R. S., Dopita M. A., 1993, *ApJS*, **88**, 253
- Theuns T., Leonard A., Efstathiou G., Pearce F. R., Thomas P. A., 1998, *MNRAS*, **301**, 478
- Totani T., Kawai N., Kosugi G., Aoki K., Yamada T., Iye M., Ohta K., Hattori T., 2006, *PASJ*, **58**, 485
- Trac H. Y., Gnedin N. Y., 2011, *Advanced Science Letters*, **4**, 228
- Trac H., Cen R., Loeb A., 2008, *ApJ*, **689**, L81
- Turner M. L., Schaye J., Crain R. A., Theuns T., Wendt M., 2016, *MNRAS*, **462**, 2440
- Vanzella E., et al., 2018, *MNRAS*,
- Viel M., Becker G. D., Bolton J. S., Haehnelt M. G., 2013a, *Phys. Rev. D*, **88**, 043502
- Viel M., Schaye J., Booth C. M., 2013b, *MNRAS*, **429**, 1734
- Wiersma R. P. C., Schaye J., Theuns T., Dalla Vecchia C., Tornatore L., 2009, *MNRAS*, **399**, 574
- Wise J. H., Demchenko V. G., Halicek M. T., Norman M. L., Turk M. J., Abel T., Smith B. D., 2014, *MNRAS*, **442**, 2560
- Worseck G., et al., 2014, *MNRAS*, **445**, 1745
- Worseck G., Prochaska J. X., Hennawi J. F., McQuinn M., 2016, *ApJ*, **825**, 144
- Wyithe J. S. B., Bolton J. S., 2011, *MNRAS*, **412**, 1926
- Zackrisson E., Rydberg C.-E., Schaerer D., Östlin G., Tuli M., 2011, *ApJ*, **740**, 13

This paper has been typeset from a $\text{\TeX}/\text{\LaTeX}$ file prepared by the author.